The high-frequency dynamics of liquid water

1999 J. Phys.: Condens. Matter 11 R259

(http://iopscience.iop.org/0953-8984/11/24/202)

J. Phys.: Condens. Matter **11** (1999) R259–R293. Printed in the UK PII: S0953-8984(99)91316-4

REVIEW ARTICLE

The high-frequency dynamics of liquid water

Giancarlo Ruocco† and Francesco Sette‡

† Universitá di L'Aquila and Istituto Nazionale di Fisica della Materia, I-67100, L'Aquila, Italy
‡ European Synchrotron Radiation Facility, BP 220, F-38043 Grenoble Cédex, France

Received 8 February 1999

Abstract. This article is dedicated to reviewing the recent inelastic x-ray scattering (IXS) work on the high-frequency collective dynamics in liquid water. The results obtained with the IXS technique are directly compared with existing ones from inelastic neutron scattering (INS) and molecular dynamics simulation investigations that were carried out with the aim of achieving an understanding of the collective properties of water at the microscopic level. The IXS work has made it possible to demonstrate experimentally the existence, in the range of exchange momentum (Q) examined (1–10 nm^{-1}), of two branches of collective modes: one linearly dispersing with Q (with the apparent sound velocity of $\approx$3200 m s^{-1}) and the other at almost constant energy (5–7 meV). It has been possible to show that the dispersing branch originates from an upwards bend of the ordinary sound branch observed in low-frequency measurements. The study of this sound velocity dispersion, marking a transition from the ordinary sound, c_o, to the 'fast' sound, c_∞, as a function of temperature, has made it possible to relate the origin of this phenomenon to a structural relaxation process, which presents many analogies with those observed for glass-forming systems. The possibility of estimating from the IXS data the value of the relaxation time, τ, as a function of temperature leads to a relating of the relaxation process to the structural rearrangements induced by the making and breaking of hydrogen bonds. In this framework, it is then possible to recognize a hydrodynamical 'normal' regime, i.e. one for which the density fluctuations have a period of oscillation that is on a timescale that is long with respect to τ, and a solid-like regime in the opposite limit. In the latter regime, the density fluctuations 'feel' the liquid as frozen and the sound velocity is much higher: this is 'fast' sound, whose velocity is equivalent to the sound velocity found in crystalline ice I_h.

1. Introduction

The investigation of the collective dynamics in liquids, and fluid systems in general, has constituted a very active field of research since the beginning of modern science. The absence of translational invariance, as well as the interplay between the collective properties such as density, charge, and concentration fluctuations, and other phenomena such as particle diffusion, particle rotations, and the degrees of freedom associated with the internal structure of the particle itself, are inherent to the fluid state. In fact, they lie at the origin of many macroscopic properties which are characteristic of the fluid, and differentiate this state of matter from the solid and, in particular, from the crystalline phases. These properties have stimulated many efforts, both theoretical and experimental, to characterize the dynamical and structural properties of fluids over the widest possible regions of time and length. In this respect, the *relaxation* process is one of the most important concepts for the understanding of the atomic dynamics in fluids. In its definition, it contains intrinsically a temporal and/or a spatial notion that, for a specific relaxation process, implies a characteristic time τ_R and/or a characteristic length ξ_R. The dynamical properties of the fluid will be noticeably different according to

0953-8984/99/240259+35$19.50

whether one considers dynamics that have a timescale and/or length scale (i) long or (ii) short with respect to τ_R and/or ξ_R for the relaxation process considered. In turn, in the same fluid, there can be different relaxation processes that may have characteristic time domains that are well separated, or ones that overlap in some common region, giving rise to interesting cooperative phenomena. The study of the density (charge, concentration, ...) fluctuations provides a direct means for identifying the presence and the character of a relaxation process. Moreover, studies of the relaxation as a function of the thermodynamic state of the fluid may allow one to understand the physical origin of the relaxation process itself.

A key quantity, from both theoretical and experimental points of view, for the determination of the collective dynamics associated with density fluctuations is the dynamical structure factor, $S(Q, E)$. It is defined as the Fourier transform in space and time of the particle-density pair correlation function:

$$S(Q, E) = \frac{1}{2\pi}\frac{1}{N}\sum_{I_N} p_{I_N}\int \mathrm{d}t\ \mathrm{e}^{\mathrm{i}Et/\hbar}\sum_{m,n}\langle I_N|\mathrm{e}^{\mathrm{i}\boldsymbol{Q}\cdot\boldsymbol{R}_m(t)}\mathrm{e}^{-\mathrm{i}\boldsymbol{Q}\cdot\boldsymbol{R}_n(0)}|I_N\rangle. \tag{1}$$

Here N is the number of particles in the system whose positions at time t are $R_n(t)$ ($n = 1, \ldots, N$). $|I_N\rangle$ is a state of the system, while the sum over these states, each with population p_{I_N}, gives the statistical average.

$S(Q, E)$, being the power spectrum in energy E of the Q-component of the density fluctuations $\rho_Q(t)$,

$$\rho_Q(t) = \frac{1}{\sqrt{N}}\sum_n \mathrm{e}^{\mathrm{i}\boldsymbol{Q}\cdot\boldsymbol{R}_n(t)} \tag{2}$$

exhibits features of both E and Q which correspond to the characteristic excitations of the system. From the theoretical point of view, one can derive the general expression for $S(Q, E)$ in two limit cases, corresponding either to $Q \to 0$ or to $Q \to \infty$. In the first case, one considers the medium as a continuum and the excitations on so long a timescale that the system can be assumed to be in thermodynamical equilibrium. Under such approximations, one builds up the hydrodynamics theory from the equations of conservation of energy, momentum, and number of particles. The solution is found for a specific system by means of another set of equations, the constitutive equations, that, by introducing transport coefficients such as the bulk and shear viscosities and the heat conductivity, allow one to derive an explicit expression for $S(Q, E)$ [1–3]. This is constituted of three lines, referred to as the Brillouin triplet, which are centred at $E = 0$ and $E = \pm\hbar c_o Q$, and correspond respectively to the entropy fluctuations and to the compression wave propagating with the adiabatic sound velocity c_o. The two lines at $E = \pm\hbar c_o Q$ correspond to the energy loss and energy gain, and have a width

$$(D_V + (\gamma - 1)D_T)Q^2$$

controlled by the longitudinal kinematic viscosity D_V, the thermal diffusion coefficient D_T, and the specific heat ratio γ. The width of the line centred at $E = 0$ is proportional to $D_T Q^2$. In the opposite limit of $Q \to \infty$, one assumes the validity of the impulse approximation, where the final state of the excited particle has a kinetic energy much higher than the potential energy, and the wavefunction is therefore well represented by a plane wave. Under these conditions, the lineshape of $S(Q, E)$ reflects the initial-state momentum distribution, i.e., in a classical fluid, the Boltzmann distribution. Then $S(Q, E)$ reduces to a Gaussian centred at the recoil energy $\hbar^2 Q^2/2M$, with standard deviation

$$\sigma = \hbar Q\sqrt{K_B T/M}$$

where M is the particle mass. In this limit, the dynamics becomes that of free particles between successive collisions. In these two extreme limits, reflecting idealized situations, one

can neglect the details of the interactions among particles and their effects on the dynamics. On the other hand, the wish to obtain an understanding of these interactions constitutes the main motivation of modern studies on the dynamics of fluids and disordered systems in general.

The investigation of the collective dynamics in disordered systems, away from the hydrodynamic and single-particle limits outlined above, becomes of particular interest when one considers an intermediate timescale and an intermediate length scale—more specifically, when one considers distances comparable to those that characterize structural correlations among particles, and times comparable to the lifetimes of these correlations. On this intermediate scale, one expects to observe a large modification of the dynamics when the times considered are either much longer or much shorter with respect to those required by the system to relax from a spontaneous density fluctuation back into its equilibrium state.

The dynamics in this intermediate region is studied, theoretically, by attempting to extend the hydrodynamics theory to small distances and short times, numerically, employing simulation methods based on the integration of the equations of motion of an ensemble of particles interacting via a specific model potential, and, experimentally, by using scattering methods to determine the dynamic structure factor directly.

Quite generally, as long as one considers Q-transfers that are small with respect to $Q_m \approx 2\pi/d$, where d is the mean interparticle distance and Q_m is the Q-value corresponding to the first maximum in the static structure factor $S(Q)$, one finds that $S(Q, E)$ preserves a three-mode lineshape as in the hydrodynamic limit. This behaviour is predicted by the generalized hydrodynamics and by the molecular hydrodynamics theories, obtained as a generalization of the hydrodynamics theory by making the assumption of a Q- and E-dependence of the parameters entering into the constitutive equations. Technically, this is accomplished by the introduction of the memory function formalism, which allows one to find evidence for the coupling between the density fluctuations and the relaxation processes active in the system. The continuous evolution from the Brillouin triplet in the hydrodynamic limit towards a more complex triplet has been found in a large number of molecular dynamics (MD) simulations. For example, in the case of simple monatomic fluids, this evolution has been confirmed by several MD studies performed with both hard spheres [4] and Lennard-Jones potentials [5]. Experimentally, using Brillouin light scattering (BLS) spectroscopy, one can study $S(Q, E)$ up to Q-values of the order of 0.04 nm^{-1}, i.e. well within the expected range of validity of the hydrodynamics theory. However, even in this small-Q range, one finds the need for energy-dependent transport coefficients to be associated with the presence of a relaxation process with a characteristic time τ in the *nano*second range. This need manifests itself in the modifications of the Brillouin linewidth and of the speed of sound from the hydrodynamic value c_o to a higher value c_∞, when the excitation frequency $E/\hbar$ is comparable with $1/\tau$: the dispersion of c is typically observed on changing the thermodynamic state of the system (T), and therefore τ.

The extension to larger Q- and E-values, and in particular up to $Q \approx Q_m$, had been experimentally more difficult until inelastic x-ray scattering (IXS) spectroscopy with meV energy resolution was developed. The highly developed inelastic neutron scattering (INS) technique cannot be easily applied at Q-transfers smaller than 10 nm^{-1} for typical liquid systems because the required energy transfers are too large for standard INS spectrometer set-ups.

In this article we aim to give a review on our present understanding of the high-frequency collective dynamics in liquid water. This study has benefited from the experimental work performed using the IXS method, which has made it possible to determine $S(Q, E)$ experimentally over a wide range of temperatures and pressures in the 1–20 nm^{-1} Q-transfer range, i.e. up to $Q_m = 20$ nm^{-1} from well below that value. We are interested here in the 'normal'-liquid state, and we will not enter into the very interesting debates (i) on the

anomalies of liquid water [6], such as the origin of the density maximum at $T = 4\ ^{\circ}\mathrm{C}$ and of the specific heat increasing with decreasing temperature in the supercooled region, (ii) on the existence of a spinodal transition [7], and (iii) on the presence of a second critical point which would allow, in water, the existence of one glassy and two liquid phases [8]. It is our hope that a good understanding of the dynamics of normal water, considered to be in the liquid phase at temperatures T above the melting point, may also contribute to the understanding of these anomalies. Our aim, however, is to determine experimentally the high-frequency dynamics in this very important hydrogen-bonded liquid, and to relate the results to the dynamics of crystalline ice, to liquid water in the hydrodynamic limit, and to the phenomenology characteristic of other liquid systems in the presence of a relaxation process.

Further motivation for the present work is provided by the long-standing issue of the existence of a fast-sound mode in liquid water. This mode, whose sound velocity is more than twice that of ordinary sound, was predicted by MD simulations and some INS experiments. Its existence, in addition to the low-temperature anomalies, has contributed to water being considered to be a quite special system.

The main topics that we will review and address in this article are:

(a) The experimental study of this fast-sound mode, and the determination of the Q-region where it exists.
(b) The relation of this mode to the tetrahedral local structure of water, and to the longitudinal acoustic dynamics in the crystalline phase of 'normal' hexagonal ice $\mathrm{I_h}$.
(c) The relationship to the ordinary sound mode, and the evolution from the hydrodynamic behaviour to that observed in the $Q \approx Q_m$ region.
(d) The comparison of the IXS results with the body of MD simulations on liquid water, and with existing data taken using the BLS and INS methods.

This effort will summarize the IXS work on this topic, and will try to put it in perspective with other methods, and with the previous knowledge on the arguments considered.

It is our hope that the reader will be convinced that this work on the high-frequency dynamics in liquid water has clarified many aspects of the collective dynamics of this system. In particular, we will show that the transition from ordinary to 'fast' sound is the consequence of a structural relaxation process, and that it is possible to 'read' the water dynamics in the same framework as is utilized for glass-forming liquids. This structural relaxation process is characterized by a relaxation time, τ, whose value, estimated from the IXS data, strongly depends on the thermodynamic state of the system. This time is shown to be related to the formation and breaking of hydrogen bonds. The density fluctuations on a timescale short with respect to τ propagate in a 'rigid' network of molecules bound to each other by hydrogen bonds, and therefore the dynamics is very similar to that in the solid phase. This is characterized by a 'fast' velocity of sound, and one can observe it in the liquid excitations whose origin can be related to the transverse phonons in the crystal. In the other limit, when the density fluctuations are slow with respect to τ, and therefore the molecules have time to rearrange themselves after the action of the perturbation (the local change of density associated with the propagating density fluctuation), the fluctuations 'feel' an average, rather than an instantaneous, structure, and the system behaves as a normal liquid.

The article is organized into seven more sections. In the next section we will summarize the knowledge that existed on the high-frequency dynamics in liquid water before the beginning of the IXS work. In section 3 we will introduce the inelastic x-ray scattering method and its capabilities in the study of the collective dynamics in disordered systems. In section 4 we will report the IXS data on liquid water at ambient conditions, which show the existence of the fast-sound mode and, on the basis of the small isotope shift between H_2O an D_2O, prove that

this mode is a centre-of-mass property. In section 5, the results for the liquid are compared to those for the solid, and this will highlight a striking equivalence between the high-frequency longitudinal dynamics of the two phases. Moreover, this comparison will allow us to relate a feature observed in $S(Q, E)$ for the liquid to the transverse dynamics in the solid, and this will make the equivalence between the two systems even more evident in the momentum- and energy-transfer regions considered. In section 6, the IXS data are compared to a large-scale MD calculation, and this analysis will substantiate even more the finding that, once the 'fast'-sound regime is reached, the liquid has a collective dynamics very similar to that of a solid, and even shows a transverse dynamics that in a normal liquid is expected to be only relaxational-like. In section 7, we will address the very important point of the origin of the relaxation process responsible for the transition from c_o to c_∞. The study of the transition as a function of temperature at constant density in the -20–300 °C temperature range will allow us to identify a phenomenology very similar to the one commonly observed for glass-forming liquids in the Q–E range typically spanned in BLS experiments. The observed temperature dependence of the transition $c_o \rightarrow c_\infty$ can be interpreted, in fact, in terms of the existence of a structural (α-) relaxation. The analysis of the energy of the excitations as a function of Q and T will allow us to derive the values of τ which do lead to an Arrhenius behaviour in the temperature range considered, and for which the energy is comparable to the hydrogen bond energy. These findings will bring us to the conclusions of the article, summarized in the last section. They lead us to believe that the high-frequency dynamics of liquid water can be successfully described in the same framework as that utilized for glass-forming liquids, and that it is the formation and breaking of hydrogen bonds that leads to the difference between the dynamics observed at high (solid-like) momentum transfers and that observed at low (liquid-like) momentum transfers.

2. The high-frequency dynamics in liquid water

In 1974 Rahman and Stillinger [9], while analysing the results of their molecular dynamics simulations on liquid water, discovered the existence of two modes in $S(Q, E)$ in the 3–6 nm^{-1} Q-region. These modes were found at energies such that, if associated with propagating modes $E/\hbar = cQ$, they would give velocities of sound $c \approx 1500$ m s^{-1} and ≈ 3000 m s^{-1}. The first value is similar to the ordinary speed of sound in water at ambient conditions. The mode giving the other value, which also showed the most marked linear dispersion in Q, was, at that time, interpreted as a band of excitations associated with the hydrogen-bond network, and propagating with a much higher sound velocity: the 'fast' sound. These observations were limited to a small Q-region, probably too small to firmly establish the effective existence of a linear relation between peak energy and momentum of the excitations in the two branches, $E/\hbar = cQ$.

The simulation experiment of Rahman and Stillinger, whose results are reported in figure 1, stimulated a lot of interest in this issue, motivating further simulation work, as well as attempts to experimentally determine $S(Q, E)$ in the region of interest. Two experimental determinations of the coherent dynamic structure factor of liquid D_2O were in fact performed using neutron spectroscopy, in 1978 and in 1985. The first one was executed by Bosi and collaborators [10] using a triple-axis spectrometer on the TRIGA reactor (Enea-Casaccia, Rome, Italy). The kinematics region explored in this experiment, however, did not allow the excitations branch associated with the fast sound to be reached. The low-energy band was nevertheless observed, but, as seen in figure 1, it showed a very weak Q-dependence. The excitation energy observed at the lowest Q-value of 5 nm^{-1} is consistent with a speed of sound of 1500 m s^{-1}, and therefore with the low-energy mode of the Rahman and Stillinger MD

simulation. In a second experiment, performed in 1985 by Teixeira and collaborators [11] on the IN8 spectrometer at the ILL (Grenoble, France), the use of higher-energy neutrons allowed the extension of the kinematics region up to that of the expected dispersion law of the fast sound. In this experiment it was indeed possible to demonstrate the existence of a collective excitation propagating with $c \approx 3300$ m s^{-1} in the $Q = 3.5$–6 nm^{-1} region. The low-energy band seen by Bosi *et al* [10], however, was not observed in this second experiment, because of the limited energy resolution ($\Delta E = 4.5$ meV) and the large quasi-elastic contribution.

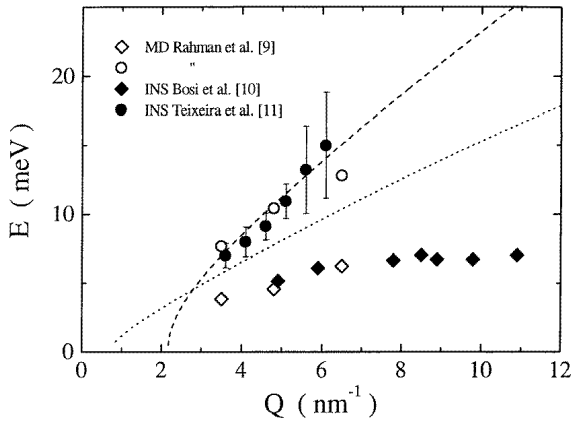

Figure 1. The open symbols represent the excitation energies for the normal (open diamonds) and *fast* (open circles) sound found by Rahman and Stillinger [9] by MD simulation with the ST2 potential. The full symbols (full diamonds [10]; full circles [11]) are the corresponding experimental findings. The dashed and dotted curves are the kinematics limits of the inelastic neutron scattering experiments for the incident neutron energy and the minimum scattering angle utilized in the two experiments. Only the E–Q region that lies below the curves can be accessed experimentally. The dashed curve indicates the upper limit of the kinematics region of the experiment of Bosi *et al* [10]; it is clear that the high-frequency mode was not accessible. The dotted curve indicates the upper limit of the kinematics region accessible to the experiment of Teixeira *et al* [11], where $E_i = 80$ meV and $\theta = 2^\circ$. It is evident that in this case the additionally accessible region is very valuable for getting information on the pattern of the excitations in liquid water. However, the increased energy resolution (4.5 meV), as a consequence of the higher energy of the incoming neutrons, was not sufficient to allow one to detect the low-energy mode in this experiment.

In figure 1, together with the MD and INS data, we also report the kinematics limits of the two neutron experiments. In the experiment of Bosi *et al* [10] the kinematics limit imposed by the scattering geometry and the neutron energy utilized was such that it was not possible to access the high-energy excitations. In the experiment of Teixeira *et al* [11] it was possible to access the fast-sound mode in the 3.5–6 nm^{-1} Q-range, but, with an energy resolution of 4.5 meV, it was not possible to detect the low-energy mode at the same time.

These results were followed by a large number of numerical simulations [12–21], carried out with the aim of clarifying the origin of the fast sound, and, in particular, of assessing whether, at high frequencies, there are two independent propagating collective dynamics in liquid water, and establishing what the relationship between the fast-sound mode and the ordinary sound branch observed at low Q-values is. The results of these MD simulations can be summarized as follows:

- The low-energy branch found by Rahman and Stillinger, in agreement with the experimental data of Bosi *et al*, has an energy $E = 4$–6 meV, and its dispersion with

Q is very weak. This branch is more evident in those simulations that utilize potential models that tend to overestimate the tetrahedral structure of liquid water, such as the ST2 and SPC models. This band has been tentatively assigned to an O–O–O-bending localized vibration [16].

- It is not possible to exclude the possibility that the high-energy branch, arising from a collective dynamics propagating with a speed of sound of $\approx$3300 m s^{-1}, is the form of the normal-sound branch that evolves at high frequency, observed in the $Q = 0$ limit, where it propagates with a speed of sound of $\approx$1500 m s^{-1}. Such dispersion with Q of the sound velocity may have its origin in the details of the intermolecular interaction, and its large value may be due to the strong electrostatic O–H intermolecular interaction, leading to an average O–O distance well below the Lennard-Jones σ-value for oxygen atoms [18].
- The analysis of the partial structure factors $S_{OO}(Q, E)$ and $S_{HH}(Q, E)$ indicates that the hydrogen dynamics is confined to much higher energies (above 50 meV), and therefore it is unlikely to be associated with the fast-sound branch [15].

The hypothesis that the fast sound is simply the continuation to high Q-values of the normal sound is sustained by comparison with other liquids, and in particular with glass-forming liquids. In these systems one observes systematically a jump in the sound velocity at Q-values such that the excitation frequency is comparable to the inverse of the relaxation time. Indeed, an analysis in this direction of the Brillouin light scattering spectra for H_2O [22, 23] confirms this possibility, predicting a large increase in the speed of sound at high Q.

Fairly recently, another neutron experiment was performed, in 1994, on the spectrometer MARI at the RAL (Chilton, Didcot, UK) [24]. Limitations on the available kinematics region, however, again prevented information on the fast-sound branch from being obtained. Nevertheless, it confirmed the results obtained sixteen years before by Bosi *et al* [10].

In figure 2, we summarize in the plane Q–E the positions of the excitations in liquid water as derived from selected MD studies and from the neutron experiments. We also report, as a chain line, the linear dispersion that one would find if the speed of sound in the high-frequency

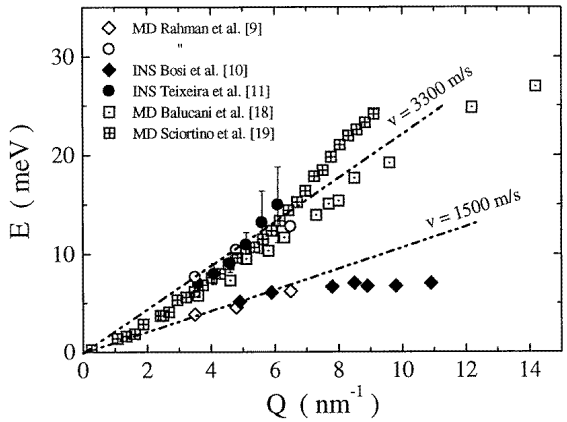

Figure 2. The excitation energies for the *fast*-sound mode derived from selected MD studies (dotted squares [18]; crossed squares [19]) are reported as functions of Q together with the corresponding quantities from figure 1 (open and full symbols). The two lines are the dispersion relations expected for the continuation to high Q of the hydrodynamic sound modes ($\approx$1500 m s^{-1}) and the *fast*-sound dispersion derived from the experiment of Teixeira *et al* [11] ($\approx$3300 m s^{-1}).

region were to be the same as that in the $Q = 0$, limit, i.e. the ordinary sound $c_o = 1500\ \mathrm{m\,s^{-1}}$.

In summary, the situation up to 1994 was not satisfactory or clear. The reason for this was, on the one hand, the large scatter of results in the numerical simulation work for different interaction potential models, and, on the other hand, the kinematics limitations of the neutron spectroscopy studies, which prevented simultaneous access to the Q–E regions of the two branches. This would have provided definitive evidence for the existence of the two modes, and it would have allowed the instigation of an experimental investigation aiming to reveal their origin, and, more generally, their relation to the properties of the liquid state. Within this context, the use of x-rays as a spectroscopic probe alternative to neutrons can give, and in fact has given, important new information on the problem. With this motivation, the IXS technique has been applied to study the high-frequency dynamics of liquid water, and this work will be reviewed in the following sections.

3. Inelastic x-ray scattering with *milli*-electron volt energy resolution

The study in condensed matter physics of atomic density fluctuations on the scale of interparticle separations is, traditionally, the domain of neutron spectroscopies. The principal reason for which neutrons are particularly suitable for these studies is the very good matching between the phase space of thermal neutrons and that of phonon-like collective excitations. In fact, the energies of neutrons with wavelengths of the order of interparticle distances are about 100 meV, and this value is comparable to the energies of phonons with wavelengths in the *nano*metre range. As a consequence, one can determine $S(Q, E)$ without requiring an excessive relative energy resolution in the spectrometers, and therefore one utilizes very efficiently the intensity of the source.

In principle, x-rays can also be used to determine $S(Q, E)$. The inelastic x-ray scattering cross-section, under certain circumstances, has an expression formally very similar to that valid for neutrons, and the coupling of x-rays and neutrons to the density fluctuations is of the same order of magnitude. This can be understood by considering the complementarity between x-ray and neutron Bragg diffraction, and extending it to the dynamics, i.e. to the density fluctuations around the static structure. The x-ray scattering cross-section is derived by considering the interaction between the electrons and the x-ray electromagnetic field. In the weak relativistic limit, the interaction Hamiltonian is composed of four terms. Two describe the diamagnetic (the Thomson term) and paramagnetic (the photoelectric absorption term) coupling of the photon field to the electron current. The other two, considerably smaller, describe the magnetic couplings. In the present context we will consider only the charge scattering arising from the Thomson interaction Hamiltonian, which requires us to utilize an x-ray energy sufficiently far away from the photoabsorption edges of the core lines for the system investigated. The Thomson interaction Hamiltonian, H_{Th}, is given by

$$H_{Th} = \frac{1}{2} r_o \sum_j A^2(\boldsymbol{r}_j, t). \tag{3}$$

Here $r_o = e^2/mc^2$ is the classical electron radius, and $A(\boldsymbol{r}_j, t)$ is the vector potential of the electromagnetic field at r_j, the coordinate of the jth electron. The sum extends over all of the electrons in the system. The double-differential cross-section is proportional to the number of incident probe photons which are scattered with an energy and momentum variation within an energy range ΔE and a solid angle $\Delta\Omega$. Considering an event where a photon of energy E_i, wavevector $\boldsymbol{k}_i$, and polarization $\boldsymbol{\epsilon}_i$ is scattered into a final state of energy E_f, wavevector $\boldsymbol{k}_f$, and polarization $\boldsymbol{\epsilon}_f$, while the electron system goes from the initial state $|I\rangle$ to the final state

$|F\rangle$, the double-differential cross-section is

$$\frac{\partial^2\sigma(E,\Omega)}{\partial\Omega\,\partial E} = r_o^2(\boldsymbol{\epsilon}_i\cdot\boldsymbol{\epsilon}_f)^2\frac{k_f}{k_i}\sum_{I,F}p_I\left|\langle I|\sum_j \mathrm{e}^{\mathrm{i}\boldsymbol{Q}\cdot\boldsymbol{r}_j}|F\rangle\right|^2\delta(E-E_i+E_f) \tag{4}$$

where $\boldsymbol{Q}=\boldsymbol{k}_i-\boldsymbol{k}_f$ is the momentum transfer to the system. The sum over the initial and final states is the statistical average, and p_I corresponds to the population of the initial state. From this expression, which implicitly contains the dynamic structure factor of the electron density, one obtains the correlation function of the atomic density on the basis of the following considerations:

(a) We assume the validity of the adiabatic approximation. This allows us to separate a quantum state $|S\rangle$ of the system into the product of an electronic part, $|S_e\rangle$, which depends only parametrically on the nuclear coordinates, and a nuclear part, $|S_N\rangle$: $|S\rangle=|S_e\rangle|S_N\rangle$. This approximation is particularly good for excitation energies that are small with respect to the excitations energies of electrons in bound core states: considering the energy of typical phonon excitations, this is indeed the case in basically any atom. For metals, one neglects the small portion of the total electron density near the Fermi level.

(b) We limit ourselves to considering the case in which the electronic part of the total wavefunction is not changed by the scattering process, and therefore the difference between the initial state $|I\rangle=|I_e\rangle|I_N\rangle$ and the final state $|F\rangle=|F_e\rangle|F_N\rangle$ is due only to excitations associated with atomic density fluctuations.

Using these two hypotheses one obtains

$$\frac{\partial^2\sigma(E,\Omega)}{\partial\Omega\,\partial E} = r_o^2(\boldsymbol{\epsilon}_i\cdot\boldsymbol{\epsilon}_f)^2\frac{k_f}{k_i}\sum_{I_N,F_N}p_{I_N}\left|\langle I_N|\sum_n f_n(Q)\mathrm{e}^{\mathrm{i}\boldsymbol{Q}\cdot\boldsymbol{R}_n}|F_N\rangle\right|^2\delta(E-E_i+E_f) \tag{5}$$

where $f_n(Q)$ is the atomic form factor of the atom n, which is the Fourier transform in space of the atomic electronic charge density, obtained by carrying out in equation (3) the integration over the electron coordinates of the electronic ground-state expectation value for this quantity. Assuming that all of the scattering units in the system are equal, this expression can be further simplified by factorization of the form factor of these scattering units. By the introduction of the dynamic structure factor $S(Q,E)$ as defined in equation (1), the double-differential cross-section for IXS from atomic density fluctuations reduces to the following expression:

$$\frac{\partial^2\sigma(E,\Omega)}{\partial\Omega\,\partial E} = r_o^2(\boldsymbol{\epsilon}_i\cdot\boldsymbol{\epsilon}_f)^2\frac{k_f}{k_i}|f(Q)|^2S(Q,E). \tag{6}$$

In the limit $Q\to 0$, the form factor is equal to the number of electrons localized on the scattering atom, Z. On increasing the value of Q, the form factor decays rapidly with a decay constant for each electron of the order of the inverse of its electronic shell dimension. At Q-values large with respect to these dimensions, therefore, the inelastic x-ray scattering from density fluctuations is strongly reduced. The cross-section derived so far is valid for a system composed of a single atomic species. Equation (5), however, can easily be generalized to molecular or crystalline systems by substituting for the atomic form factor with either the molecular form factor or the elementary cell form factor, respectively. The situation becomes more involved if the system is multi-component and disordered. In this case the factorization of the form factor is still possible, but only if one assumes some correlated distribution among the different atoms. In the limit case where the distribution is completely random, an incoherent contribution appears in the scattering cross-section, exactly as in the case of neutron scattering [25].

We remark that the strength of the coupling of the x-rays to the electrons in the derived cross-section is determined by the square of the classical electron radius, $r_o=2.82\times10^{-13}$ cm.

This strength is comparable to that determining the neutron–nucleus scattering cross-section, r_o being comparable to b, the nuclear scattering length [25].

In spite of the strong analogies between inelastic neutron and x-ray scattering, the development of the x-ray method has so far been limited, mainly for the following reasons:

- Photons with wavelength $\lambda = 0.1$ nm have energies of about 10 keV. Therefore, the study of phonon excitations in the meV region requires a relative energy resolution $\Delta E/E \approx 10^{-7}$ at least.
- The total absorption cross-section of x-rays of energy 10 keV is limited in almost all cases ($Z > 4$) by the photoelectric absorption process and not by the Thomson scattering process. The photoelectric absorption, whose cross-section is roughly proportional to Z^4, determines, therefore, the actual sample size along the scattering path. Consequently, the Thomson scattering channel is not very efficient for a system with high Z in spite of the Z^2-dependence of its cross-section (equation (5)).
- The rapid decrease (approximately exponential) of the atomic (molecular) form factor with increasing Q is responsible for a drastic reduction of the scattering cross-section, i.e. of the measured intensity, even at relatively small momentum-transfer values.

Despite these important limitations, however, there are situations where the use of x-rays has important advantages over that of neutrons. One specific case is based on the general consideration that it is not possible to study acoustic excitations propagating with a speed of sound, c, using a probe particle with a speed c_i smaller than c. This limitation is not particularly relevant in neutron spectroscopy in studies of crystalline samples. Here, the translation invariance allows study of the acoustic excitations in high-order Brillouin zones, and this overcomes the difficulty of the above-mentioned kinematics limit for phonon branches with steep dispersions. In contrast, the situation is very different for topologically disordered systems: here, with only a few exceptions, and those for a limited Q–E region, it has not been possible to determine the dynamic structure factor using neutrons. For these systems, in fact, the absence of periodicity imposes the restriction that the acoustic excitations must be measured at small momentum transfers. As seen in figure 1, in the case of water, this has prevented the measurement, with good energy resolution, of $S(Q, E)$ over sufficiently extended energy and momentum regions. This applies also to many other interesting liquids and glasses, where the speed of sound is too large for existing neutron spectrometers, and the interest is in the study of the collective dynamics in the region $Q \leqslant Q_m$.

The above arguments explain why, in the study of disordered systems, the inelastic x-ray scattering technique can be extremely valuable. The x-ray probe, in fact, does not have the kinematics limitations of neutrons, and can access the region of small momentum transfers providing that the required energy resolution is experimentally achieved. In fact, because the energy transfers for the x-ray case are small compared to the incident and scattered photon energies—$E_i \approx E_f$ and $|\boldsymbol{k}_i| \approx |\boldsymbol{k}_i|$—a given scattering angle, θ_s, completely determines the magnitude of the momentum transfer, Q, independently of the energy transfer, E:

$$\frac{Q}{k_i} = 2\sin\left(\frac{\theta_s}{2}\right). \tag{7}$$

From this relation one sees that, for phonon-like excitations, in inelastic x-ray scattering there is no limitation on the energy transfer at a given momentum transfer.

The other important advantages of the IXS method are:

(a) The cross-section is highly coherent, contrary to the case for neutrons, where sometimes it is necessary to separate *a posteriori* the coherent, $\propto S(Q, E)$, and incoherent, $\propto S_s(Q, E)$, contributions.

(b) The multiple-scattering processes are in general strongly suppressed by the photoelectric absorption process, and, taking advantage of the small beam sizes obtained with x-rays, this allows the direct measurement of the dynamic structure factor without invoking sophisticated procedures for the reduction of the raw data.
(c) The possibility of having very small beam sizes at the sample position allows the study of systems available in small quantities and/or their investigation in extreme thermodynamic conditions, such as under very high pressures and at high or low temperatures.

The above discussion illustrates how the inelastic x-ray scattering technique can be very useful, and complementary to the INS technique, although it can by no means be viewed as an alternative to the powerful neutron methodologies. In particular, it shows that the development of the x-ray method would give access to an extremely important region of the E–Q plane, and, specifically, to that of small Q-values, where the acoustic excitations have energies which are not easy to access using the neutron spectroscopies. An important effort in this direction has recently been made at the European Synchrotron Radiation Facility (ESRF) in Grenoble. There, an inelastic x-ray scattering beamline (BL21-ID16) has been recently constructed, and its performance will be briefly discussed in the remainder of this section.

An x-ray beam with high resolving power can be obtained from a white source using a Bragg reflection from a perfect crystal, constituting the monochromatization process. The largest resolving power, $(E/\Delta E)_h$, obtained from the reflection $\boldsymbol{h}$ of an ideal crystal is an intrinsic property of the crystal considered.

This quantity is deduced in the framework of the dynamical theory of x-ray diffraction [26]. Here $(\Delta E/E)_h$ is proportional to the square of the effective separation between the diffracting planes d_h, and to the form factor at $Q_h = \pi/d_h$, and is independent of the Bragg angle θ_B. Qualitatively, these results can be understood by recalling that in crystal diffraction the penetration of the x-ray beam is finite even in the absence of photoelectric absorption, as the reflectivity of the crystal planes is finite. Therefore the number of planes participating in the Bragg reflection process is also finite, and $(\Delta E/E)_h$ is inversely proportional to their number. Increased resolving powers are obtained by using reflections of increased order: this is a direct consequence of (i) the reduction of the form factor (which is the reflection coefficient for the amplitude of the electric field; see equation (5)) for increasing Q, and of (ii) the proportionality between $(\Delta E/E)_h$ and d_h^2. In order to obtain an x-ray beam with high resolving power, it is therefore necessary to use high-order Bragg reflections, and to have highly perfect crystals [27].

The geometrical conditions, like the energy resolution issues, are also important aspects if one is to use a high-order Bragg reflection efficiently. From differentiation of the Bragg law, one obtains a contribution to the relative energy resolution due to the angular divergence $\Delta\theta$ of the beam impinging on the crystal: $\Delta E/E = \Delta\theta \cot(\theta_B)$. To reach the intrinsic energy resolution of the reflection considered, it is necessary to keep

$$(\Delta E/E)_h \leqslant \Delta\theta \cot(\theta_B).$$

In typical Bragg reflection geometry, $\cot(\theta_B) \approx 1$, and, for high-order reflections with $(\Delta E/E)_h \approx 10^{-8}$, the required angular divergence should be in the 10^{-8} rad range, i.e. should take values much smaller than the collimation of x-ray beams available even at the new third-generation synchrotron radiation sources (10^{-5} rad). This geometrical configuration would induce a dramatic reduction of the number of photons Bragg reflected from the monochromator, and lead to analyser crystals within the desired spectral bandwidth. Building on the pioneer work of Bottom [28] and Maier-Leibnitz [29], an elegant solution to this problem has been found by introducing extreme backscattering geometry, i.e. the use of Bragg angles very close to 90°. This provides very small values of $\cot(\theta_B)$ ($\theta_B \approx 89.98°$ gives $\cot(\theta_B) \approx 10^{-4}$). In such a way, the range of acceptable values of $\Delta\theta$ is increased to include values well above

10^{-5} rad, which therefore become even larger than the divergences $\approx 10^{-5}$ rad typical for synchrotron radiation from undulator sources.

The requirements on the energy resolution of the monochromator and of the analyser are the same. However, the required angular acceptances are very different. The x-ray beam incident on the monochromator has the angular divergence of the x-ray source, and therefore one can use a perfect flat crystal. In the case of the analyser crystal, however, the optimal angular acceptance is dictated by the desired momentum resolution. Considering values of ΔQ in the region of 0.5 nm^{-1}, well within the range for exchange momenta (1 to 10 nm^{-1}), the corresponding angular acceptance of the analyser crystal must be $\approx$10 mrad or higher, which is again an angular range well above acceptable values, i.e. also larger than the deviation of the Bragg angle from 90°. The only way to obtain such large angular acceptances is to use a focusing system, which, however, has to preserve the crystal perfection, necessary to obtain the energy resolution. A solution consists in placing a large number of undistorted perfect flat crystals on a spherical surface, with the aim of using a 1:1 pseudo-Rowland-circle geometry with aberrations kept sufficiently low that the desired energy resolution is not degraded. This method has been utilized in the construction of the ESRF spectrometer on BL21-ID16: that is, approximately 10 000 perfect silicon crystals of surface size 0.7×0.7 mm^2 and thickness 3 mm have been glued on a spherical substrate of radius 6500 mm. This 'perfect silicon crystal with a spherical shape' is the meV energy resolution analyser of the BL21-ID16 beamline.

In figure 3 we show the main optical elements of the ESRF IXS beamline. The instrument,

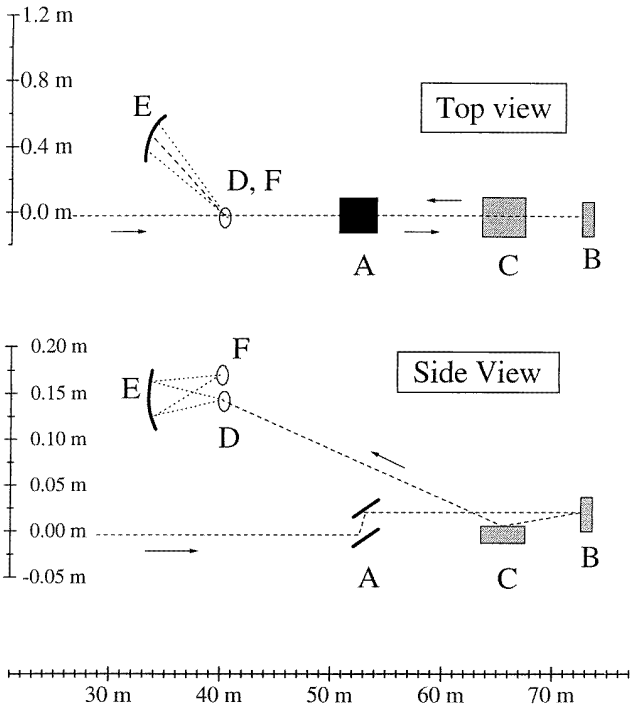

Figure 3. A schematic diagram of the layout of the inelastic x-ray scattering beamline ID16-BL21 at ESRF. The different components and their functions are sketched in the figure: (A) pre-monochromator; (B) main monochromator; (C) toroidal mirror; (D) scattering centre (sample); (E) analyser crystal; (F) detector.

a triple-axis spectrometer, has as its first element the monochromator crystal, whose role is to determine the energy, E_i, of the incident photons. The second element is the scattering sample, where one selects the scattering angle θ_s, and therefore the exchange momentum, according to equation (6). The third element is the analyser crystal, whose role is the determination of the energy E_f of the scattered photons. To maintain the backscattering geometry for any given energy transfer, a certain energy difference between the analyser and monochromator is achieved by keeping the Bragg angle constant, and by changing the relative temperature of the two crystals. This has the effect of varying the relative lattice parameter, and therefore the values of the reflected energies. Specifically, the analyser is kept at constant temperature while the monochromator temperature, and therefore E_i, is varied. Considering that $\Delta d/d = \alpha\,\Delta T$, with $\alpha = 2.56 \times 10^{-6}$ K^{-1} in silicon at room temperature, in order to obtain an energy step of about one tenth of the energy resolution, i.e. $\Delta E/E \approx 10^{-9}$, it is necessary to control the monochromator crystal temperature with a precision of about 0.5 mK. This difficult task has been achieved with a carefully designed temperature bath, controlled with an active feedback system.

The x-ray source used on the ID16-BL21 beamline is made out of two undulators. The x-ray radiation utilized is that corresponding to the undulator emission of the third, fifth or seventh harmonics, chosen to optimize the photon flux at the energies defined by the reflection order of the monochromator and analyser crystals. These are the Si(hhh) reflections, with $h = 5$, 7, 8, 9, 11, 12, 13. The x-ray beam from the undulator odd harmonics has an angular divergence of approximately 15×40 μrad full width at half-maximum (FWHM), a spectral bandwidth $\Delta E/E \approx 10^{-2}$, and an integrated power within this divergence of the order of 200 W. This beam is first pre-monochromatized to $\Delta E/E \approx 2 \times 10^{-4}$ using a Si(111) double-crystal device kept in vacuum and at the cryogenic temperature of ≈120 K (element A in figure 3). The photons from the pre-monochromator reach the high-energy-resolution backscattering monochromator (element B in figure 3). This is a flat symmetrically cut silicon crystal oriented along the (111) direction, temperature controlled with a precision of 0.2 mK over the 285–295 K temperature region. The Bragg angle at the monochromator is $\theta_B = 89.98^\circ$. The energy resolution of the x-ray beam leaving this monochromator depends on the reflection considered, and typical values are reported in table 1. The monochromatic beam impinges on a focusing toroidal mirror (element C in figure 3), which gives at the sample (element D in figure 3) a beam size of 150 (vertical) × 350 (horizontal) μm^2 FWHM. The analyser system (element E in figure 3) is made up of an entrance pinhole, slits in front of the analyser crystal to set the desired momentum resolution, the analyser spherical crystal in backscattering geometry ($\theta_B = 89.98^\circ$), an exit pinhole in front of the detector, and the detector itself (element F in figure 3). There are, in fact, five independent analyser systems at

Table 1. Measured fluxes and bandwidths of the x-ray beam leaving the high-energy-resolution monochromator on ID16-Bl21 at the ESRF at the silicon reflection orders indicated, and with 200 mA in the storage ring.

Reflection	Energy (keV)	Flux (photon s^{-1})	Resolution (meV)
5 5 5	9.885	2×10^{11}	15.0
7 7 7	13.840	6×10^{10}	5.3
8 8 8	15.816	3×10^{10}	4.4
9 9 9	17.793	6×10^{9}	2.2
11 11 11	21.748	7×10^{8}	1.0
12 12 12	23.725	3×10^{8}	0.7
13 13 13	25.702	1×10^{8}	0.5

fixed angular offsets in the scattering plane. They are mounted on an arm 7 m long that can rotate around a vertical axis passing through the scattering sample. This rotation allows one to determine the scattering angle θ_s for each of the five analysers, and therefore the corresponding exchange momentum. The arm operates between 0° and 15°. The spherical analyser crystals are kept at constant temperature with a precision of 0.2 mK, and operate at the same reflection of the monochromator in the Rowland-circle geometry with 1:1 magnification. The detectors are inclined silicon diodes with an equivalent thickness of 2.5 mm.

The performance of each of the five spectrometer channels corresponds to an energy resolution of 1.5 meV when one utilizes the Si(11 11 11) reflection [30]. At this order, the angular offset of the five analysers corresponds to an exchange momentum difference of 3 nm^{-1}. The instrumental response function of one of the five channels is reported in figure 4. This has been obtained by measuring the scattering from a disordered sample of Plexiglas at a Q-transfer corresponding to $Q = Q_m = 10\ \mathrm{nm}^{-1}$, and at $T = 20$ K, in order to maximize the elastic contribution to the scattering.

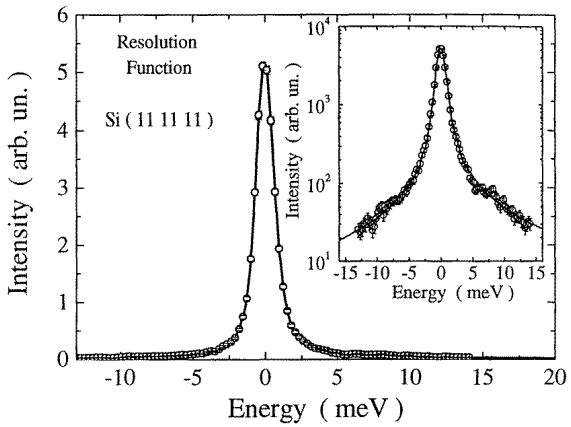

Figure 4. The resolution function of the whole instrument obtained using the monochromator and analyser Si(11 11 11) reflections in backscattering geometry and measuring the elastic scattering from a plastic sample. The analyser radius is 6.15 m. The energy scans are performed varying the relative temperature of the two crystals. The count rate is normalized to 100 mA current in the storage ring. Typical current values at the ESRF are between 100 and 200 mA. The data points are shown with statistical error bars (often the latter are smaller than the dot size). The solid curve is a Lorentzian fit to the data, and was used to determine the FWHM of the resolution function. The measured FWHM energy is 1.5 ± 0.2 meV, and was obtained with an analyser slit opening of $\approx 10 \times 10$ mrad^2. In the inset the same data are reported on a logarithmic scale to allow one to better appreciate the shape of the tail of the resolution function.

The result reported in figure 4 summarizes the best instrumental capability obtained so far from the ESRF inelastic x-ray scattering spectrometer. From this result, one can directly appreciate the value of performing IXS experiments with meV energy resolution. The remainder of this article will be dedicated to the IXS study of the high-frequency dynamics of liquid water.

4. Inelastic x-ray scattering from liquid water

The aim of clarifying our understanding of the dynamics in liquid water at high frequency, as summarized in figure 2, constitutes the main motivation of the IXS study that will be

discussed in the following. Historically, during the development and commissioning phase of the IXS spectrometer, there were three successive experiments which were performed following relevant improvements in the energy resolution of the new instrument. They were carried out in March 1995 with 5 meV energy resolution [31], in June 1995 with 3.5 meV energy resolution [32], and in February 1996 with 1.5 meV energy resolution [33]. The IXS spectra measured for liquid water at $T = 5\ ^{\circ}\mathrm{C}$ and saturated vapour pressure are reported in figure 5 as functions of the energy transfer, E, and for different values of the momentum transfer, Q. The spectra are shown together with the resolution function, obtained as in figure 4. These functions have been arbitrarily aligned at the central peak ($E = 0$), and scaled in intensity, in order to emphasize the presence of an inelastic signal whose shape and intensity changes with Q. Specifically, we observe that the energy distribution of this Q-dependent inelastic signal moves towards higher values with increasing Q.

The data reported in figure 5, as we discussed previously, directly reflect the shape of $S(Q, E)$ for liquid water in the thermodynamic state considered. In order to describe their Q- and E-dependencies, one must adopt some model function whose shape can eventually be

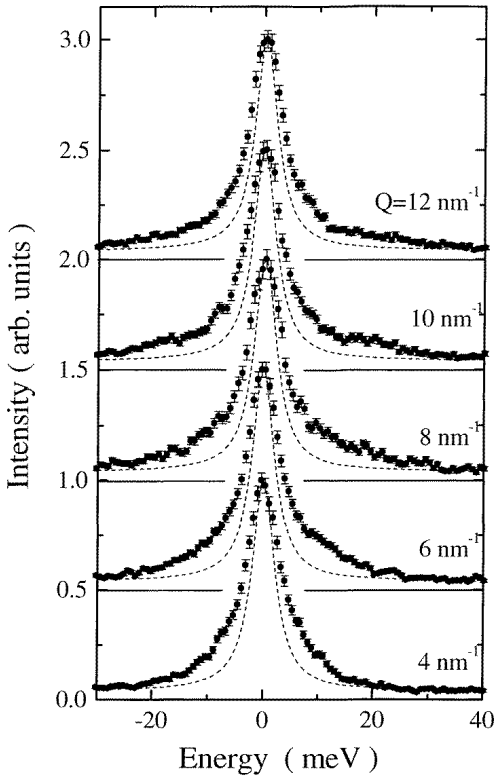

Figure 5. Inelastic x-ray scattering spectra of H_2O taken at 5 °C at the Q-values indicated. The experimental data (full circles) are shown with their the error bars. The dashed curves under the central peaks are the resolution functions (shifted upward to account for the instrumental background), shown to emphasize the Q-dependent intensity at the sides of the central peak. The data are normalized to the intensity of the central-peak maximum, and the count rates were ≈5, 4.5, 4, 4, 5, 5.5 and 6 counts s^{-1} at $Q = 4$, 5, 6, 7, 8, 9 and 10 nm^{-1} respectively. The integration time for each data point was 120 s.

justified by means of a theoretical *ansatz*. From the fit to the data, one obtains a certain number of parameters, such as the average excitation energy, the energy width, and the intensity of the inelastic signal, as well as the intensity and the width of the central peak. Following the generalized hydrodynamics theory [3], we adopted a model where $S(Q, E)$ preserves the basic features of the Brillouin triplet observed in the hydrodynamic limit: namely, a spectrum made up of a central peak and two—Stokes and anti-Stokes—inelastic features. The central peak, as in the Brillouin triplet, is modelled by a Lorentzian function, while the side peaks are represented by a damped harmonic oscillator (DHO) function [34]. The choice of the DHO function is motivated by various arguments: the first one is related to the fact that one can derive this lineshape using a Markovian *ansatz* for the memory function, i.e. one assumes that the timescale of the density fluctuations considered, and thus the reaction of the surrounding medium, is much faster than the relaxation time associated with any relaxation process active in the system. This corresponds to a model of the memory function entering in the generalized Langevin equation made up of a constant and a $\delta(t)$ function [3]. A second point is simply related to the fact that this model is routinely utilized in the analysis of neutron data and MD simulation spectra of disordered systems, and therefore its use allows a direct comparison with the existing work on liquid water. One should keep in mind, nevertheless, that this lineshape is just a model function which has been arbitrarily chosen; its main uses are to show the basic features expected for the inelastic part of $S(Q, E)$ for a disordered system in the Q-range considered, and to allow one to summarize these features and their Q- and T-dependencies using a minimal number of spectroscopic parameters, and independently of specific theories. Qualitatively similar results are obtained using other model functions for the inelastic signal, such as Lorentzians and Gaussians. The model function $F(Q, E)$ utilized is given below:

$$F(Q,E) = F_C(Q,E) + F_{DHO}(Q,E) = \frac{1}{\pi} I_c(Q) \frac{\Gamma_c(Q)}{E^2 + \Gamma_c(Q)^2} + \frac{E[n(E)+1]}{k_B T} \frac{1}{\pi} I(Q) \frac{\Gamma(Q)^2 \Omega(Q)}{(\Omega(Q)^2 - E^2)^2 + \Gamma(Q)^2 E^2}. \tag{8}$$

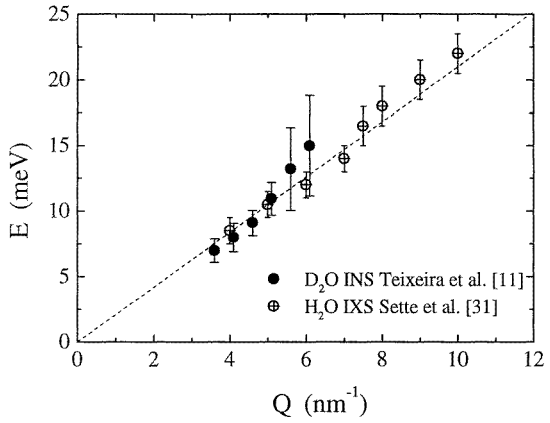

Figure 6. The excitation energy parameter, $\Omega(Q)$, as obtained from the fit to the data of figure 4 (crossed circles) is reported as a function of Q and compared with the similar quantity measured by means of INS by Teixeira *et al* [11] (full circles). The dashed line indicates the best linear fit up to 10 nm^{-1} of the IXS-derived $\Omega(Q)$, and its slope corresponds to a speed of sound of 3200 ± 100 m s^{-1}.

In this expression, $I_c(Q)$ and $I(Q)$ are the intensities of the central and inelastic contributions, $\Omega(Q)$, $\Gamma(Q)$, and $\Gamma_c(Q)$ refer to the excitation energy and to the energy widths of the side and central lines, $n(\omega)$ is the Bose factor, and k_B is the Boltzmann constant. Analytically, $\Omega(Q)$ corresponds to the maximum of the current spectrum, i.e. to the maximum of the function $E^2/Q^2 F_{DHO}(Q, E)$. The experimental spectra have been fitted to the convolution of $F(Q, E)$ with the instrument resolution function using standard χ^2-minimization routines. The values of $\Omega(Q)$ are reported in figure 6 together with the corresponding quantities derived by Teixeira *et al* from their neutron data. We observe a linear dispersion with $c = 3200 \pm 100$ m s^{-1}, and a very good overlap between the x-ray and neutron data, in spite of the fact that the neutron data were taken for D_2O and the x-ray ones for H_2O.

These x-ray measurements, when compared with the neutron data of Teixeira *et al*, allow one to clarify the following points:

(a) Over a large Q-region there is an excitation in liquid water that propagates with a velocity of sound more than double the ordinary sound velocity. The x-ray work has allowed this region to be enlarged from 3.6–6 nm^{-1} to 4–10 nm^{-1}.
(b) The energy of these excitations at a given Q is, within the error bar, equivalent for D_2O and H_2O, without an isotopic shift that can be related directly to the mass difference between

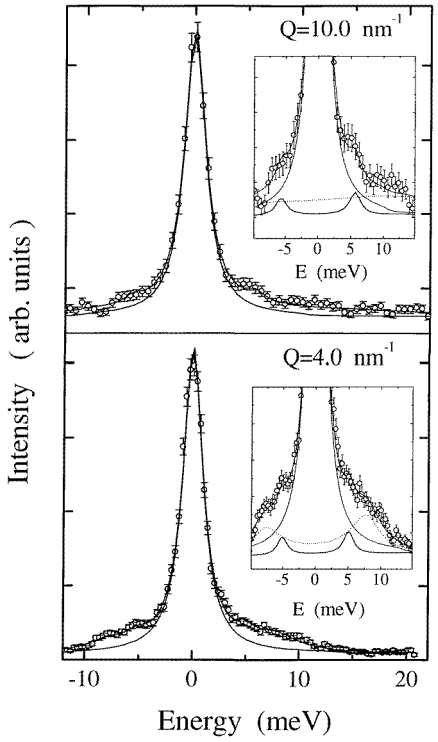

Figure 7. The IXS spectra of water at $T = 5\ ^\circ$C (open circles) shown together with the total fits and the elastic components at the Q-values indicated. The data are normalized to their maximum intensities, corresponding to 2.8 and 2.4 counts s^{-1} (total counts 1100 and 500) at $Q = 4$ and 10 nm^{-1} respectively. The insets emphasize the weakly dispersing features at ≈4–5 meV; here the experimental data are shown together with the total fit and the three individual components (elastic peak, and high- and low-energy inelastic contributions).

H and D. The x-ray studies on both D_2O and H_2O show in fact that there is a reduction of the excitation energies in D_2O with respect to those in H_2O consistent with the factor $\sqrt{18/20} \approx 0.95$ expected from the *total* mass difference between the two molecules. It is then possible to conclude that this excitation involves the centre of mass of the whole molecule, and it is not limited predominantly to the motion of the lighter hydrogen atoms.

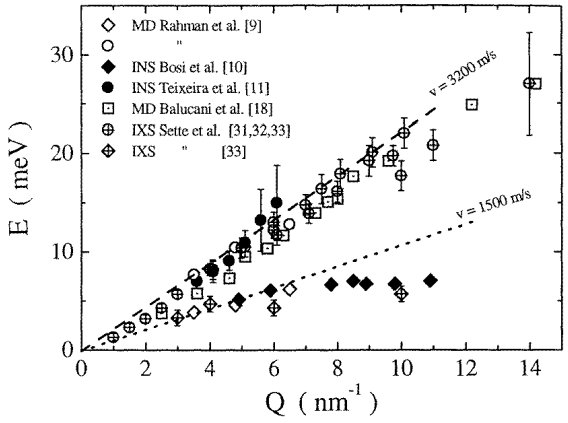

Figure 8. Excitation energies, $\Omega(Q)$ obtained using the DHO model, from the IXS experiments. The crossed circles refer to the dispersing excitation and the crossed diamonds to the weakly dispersing ones. The dashed line, with a slope of 3200 m s^{-1}, results from a fit of the IXS $\Omega(Q)$ for $Q \geqslant 4$ nm^{-1}. The dotted line is the dispersion relation expected for the continuation to high Q of the hydrodynamic sound modes (≈1500 m s^{-1}). The open and full symbols are the data already reported in figure 2.

The IXS data reported in figure 5 are dominated by the elastic peak and by the fast-sound modes. The presence of a feature at $E \approx 5$ meV, like those reported in references [10, 24], is not clear. In order to assess whether one can use IXS to observe this second excitation, the IXS spectra have been measured with increased statistical accuracy at selected Q-values. These spectra are reported in figure 7, and, beside the inelastic scattered intensity dispersing with Q, it is now possible to observe a new weakly dispersing feature with 4–6 meV energy transfer. This is emphasized in the insets of figure 7. This feature is observed only in the spectra with Q larger than 4 nm^{-1}, and is no longer detected in the spectra at small Q. Like the data in figure 5, the data at $Q \geqslant 4$ nm^{-1} were fitted by a Lorentzian for the central peak, and a DHO model for each of the two (dispersing and weakly dispersing) features. The energies of the excitations, determined from the fit and corresponding to the DHO fitting parameter $\Omega(Q)$, are reported in figure 8 together with the simulation and neutron results already reported in figure 2. The different measurements of the dispersing excitations are consistent over the common Q-range. Therefore, the IXS measurements confirm the existence of two modes in the high-frequency dynamics of liquid water at Q-values larger than 4 nm^{-1}. However, a careful study of $S(Q, E)$ at Q-values smaller than 4 nm^{-1} shows only one excitation dispersing with Q. This is apparent from the IXS data of figure 9, where it is no longer possible to observe an excitation in the 4–5 meV energy region. Most importantly, the DHO analysis of these data shows us that, in this small-Q region, there is a dispersion of the apparent velocity of sound, $c(Q) = \Omega(Q)/Q$; in fact, the value of 3200 m s^{-1} at $Q = 4$ nm^{-1} decreases to 2000 m s^{-1} at $Q = 1$ nm^{-1}. Summarizing, the IXS work and its DHO analysis, beside confirming previous studies as regards the existence of two excitations at large Q, shows that below a certain

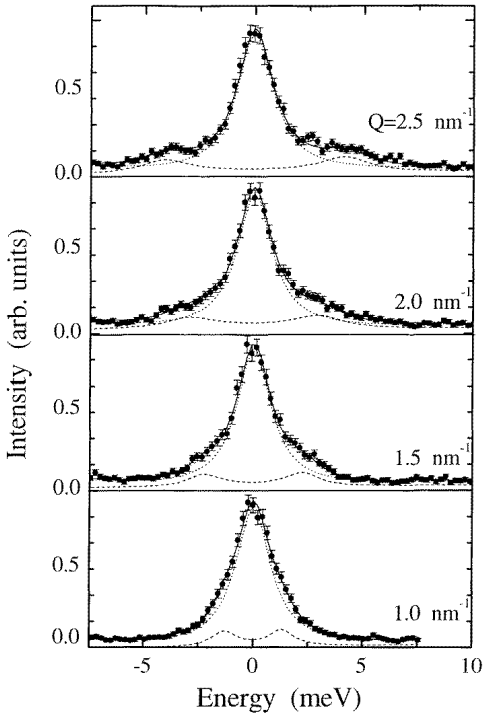

Figure 9. The IXS spectra of water at $T = 5\ ^{\circ}$C (full circles) shown together with the total fits and the individual components at the Q-values indicated. The data are normalized to their maximum intensities, corresponding to 1.4, 1.2, 1.1, 1.0 counts s^{-1} and total counts of 450, 360, 360, 350 at $Q = 1.0$, 1.5, 2.0, 2.5 nm^{-1} respectively.

Q-value only one excitation survives, and the sound velocity associated with these collective excitations progressively changes from 'fast' to ordinary values with decreasing Q-value. This experimental result, consistently with the previous finding that the 'fast'-sound mode is due to the dynamics of the centre of mass of the water molecule, implies that the 'fast' sound is the continuation to high Q of the acoustic branch mode. The Q-dependence of the apparent sound velocity is reported in figure 10.

It is important to stress that only at Q-values where the speed of sound has reached the 'fast'-sound value does one observe two modes in the spectra simultaneously. Therefore, in spite of having ascertained the existence of two modes and the dispersion of the sound velocity from the 'fast' value toward the ordinary value, very relevant questions still await clarification. Specifically: what is the mechanism leading to the transition between the two dynamical regimes in liquid water? What are the properties differentiating the high-frequency dynamical regimes from the low-frequency one, typical of ordinary hydrodynamics? What is the nature of the weakly dispersing excitation observed only at high Q-values?

5. High-frequency dynamics in solid and liquid water

The peculiarity of the large increase of the sound velocity in liquid water at high-frequency poses very basic questions regarding the nature and origin of this phenomenon. In particular, this value is comparable to the speed of sound in solid water in its most familiar crystalline

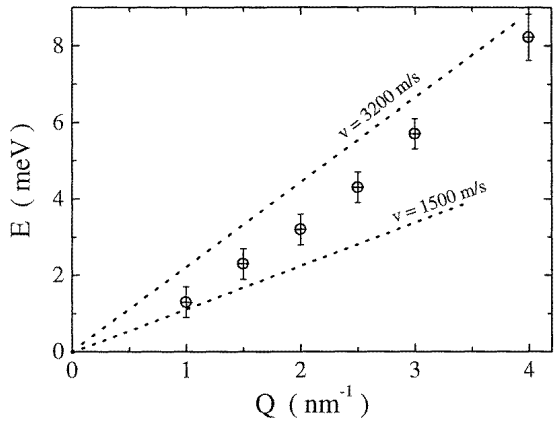

Figure 10. Excitation energies, $\Omega(Q)$ (crossed circles), in the low-Q region, where the transition from fast towards normal sound takes place, as emphasized by the two lines corresponding to the fast- and normal-sound branches.

phase: ice I_h. One may then speculate that, in a certain *time–space* domain, the density fluctuations in the liquid not only deviate from their macroscopic behaviour, but also start to become similar to those of the solid. This possibility can be explained by considering that the liquid and solid states are thermodynamical concepts related to the time evolution of the relative positions of the atoms in the condensed material considered. While in the solid there are no changes on a long timescale, the liquid undergoes characteristic structural rearrangements. These two concepts lie at the origin of many of the macroscopic properties of materials. In the microscopic limit, however, dominated by local bonding and interatomic interactions, the concepts of liquid and solid states may tend to cease to apply, and this may be one of the basic reasons for the increased sound velocity in liquid water at times in the *pico*second range and below.

Measurements of the dynamical structure factor of water in the liquid and solid states, at temperatures just above and just below the melting transition, can help one, in principle, to investigate the similarities of and the differences between the high-frequency collective dynamics of the two phases. Using the IXS method, in the present case with a total energy resolution of 3 meV, a set of measurements were performed on a solid sample kept at $-20\,^{\circ}$C. The measurements were made on different solid samples of ice I_h: polycrystals—in order to obtain an orientational averaging and thus to allow a more significant comparison with the liquid—and single crystals, along different crystallographic directions.

Inelastic x-ray scattering spectra at selected Q-values, and the corresponding fits, are shown in figure 11 for polycrystalline ice. No significant differences are found in the single-crystal spectra along the crystallographic directions investigated, $(10\bar{1}1)$ and (0001). This isotropy is a consequence of the almost perfect tetrahedral coordination among the H_2O molecules. At low Q, the spectra are dominated by the longitudinal acoustic (L) phonon branch, whose energy increases with Q. The presence of a small central peak can be attributed to residual static disorder in the crystal, and to some scattering from the air and from the windows of the sample cell. The boundary of the first Brillouin zone (BZ) in ice is at $\approx 7.5\,\mathrm{nm}^{-1}$, and below this Q-transfer value one can detect only those modes that have eigenvectors which have a finite longitudinal component. This is a consequence of the selection rule governing x-ray and neutron scattering from phonons: in order to have a finite intensity, the projection

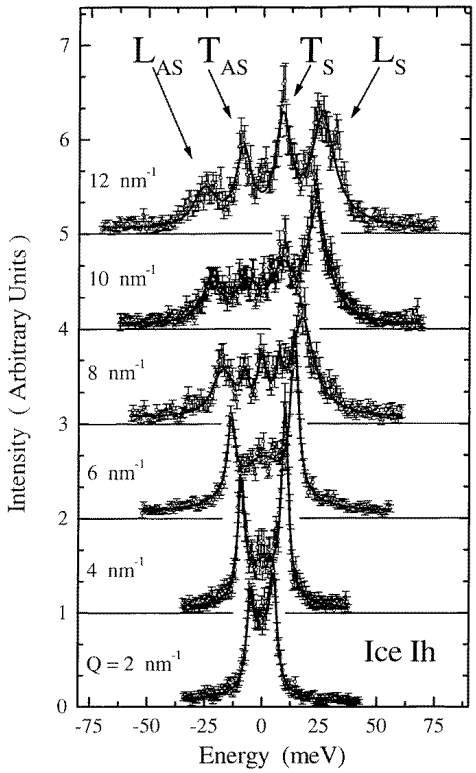

Figure 11. The IXS spectra of polycrystalline H_2O ice I_h at $-20\,^{\circ}$C, taken at the Q-values indicated with 3.2 meV and 0.4 nm^{-1} energy and momentum resolutions, are reported together with their fits. The longitudinal and transverse phonons are labelled L and T respectively. The experimental data are normalized to the maximum of the L Stokes peak. At this point, the count rates were $\approx$1 count s^{-1} at all of the Q-values investigated. The integration time for each data point was 180 s at $Q = 2$ and 6 nm^{-1} and 90 s at $Q = 10$ and 12 nm^{-1}. The data (open circles), shown with their error bars, are superimposed on the fits (solid curves). The fits were achieved by the convolution of the experimental resolution function with two pairs of Lorentzians, representing the L and T Stokes and anti-Stokes peaks. A fifth Lorentzian was used to account for the small elastic intensity probably due to residual disorder in the polycrystal.

of the phonon eigenvector along the total Q-transfer direction must be finite. Consequently, a purely transverse mode can only be detected in a BZ if it has order higher than one. Such behaviour is observed for the excitation found in figure 11 at $\approx$7 meV, which shows very little dispersion, and appears at Q-values larger than 7 nm^{-1}. In agreement with lattice dynamics calculations, this feature corresponds, in fact, to the transverse phonon branch (T), and, in the second BZ, it corresponds to what is referred to as the optical transverse phonon in the reduced-BZ representation scheme. The solid curves were obtained by fitting the spectra by the convolution of the experimental resolution function with two pairs of Lorentzians, representing the $L_{A,AS}$ and $T_{A,AS}$ Stokes and anti-Stokes peaks, and with a fifth Lorentzian to account for the elastic peak. The intensities have been normalized to the maximum of the $L_{A,AS}$ Stokes peak.

In figure 12 we report the dispersion relations for liquid and solid water as obtained from the data of figure 11 and from the IXS data already shown in figure 8. The reported energies correspond to the maxima of the longitudinal current spectra. For the crystal, this is the

maximum of the Lorentzian representing the $L_{A,AS}$ phonon. For the liquid, it is the $\Omega(Q)$ parameter of the damped harmonic oscillator model as defined in equation (7). The data for ice I_h are consistent with previous neutron measurements for D_2O performed for higher-order Brillouin zones [35].

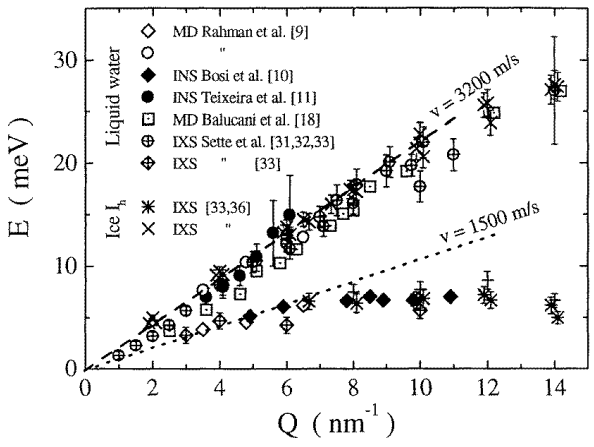

Figure 12. Excitation energies, $\Omega(Q)$, for the L (crosses) and the T (stars) excitations in polycrystalline ice I_h. The other symbols and the dashed and dotted lines have the same meaning as for figure 8.

The dispersion relations of the two modes reported in figure 12 show that there is a striking similarity between the longitudinal dynamics of liquid and solid water. These collective properties are, in fact, identical within their respective error bars. This result demonstrates that, at $Q \geqslant 4$ nm^{-1}, the collective dynamics of liquid water is equivalent to that of solid ice. This observation has at least two very important consequences. The first one is that, in the high-frequency domain considered, the density fluctuations in the liquid propagate in a 'rigid' structure imposed by the tetrahedral coordination among the water molecules, as in the solid. A second one is that, in analogy with the solid, in the liquid state there is also a transverse dynamics which shows up at Q-values higher than the one that characterizes the transition from the liquid-like to the solid-like dynamical regimes: the transition from ordinary to 'fast' sound. Contrary to the case for the crystalline phase, however, where the translational invariance allows a pure transverse dynamics, in the liquid, the absence of translational symmetry imposes the restriction that a mode cannot be purely transverse or longitudinal. This may explain why the weakly dispersing mode in liquid water, although reminiscent of the transverse phonon in the solid, always has a longitudinal component. Thanks to this longitudinal symmetry, one can observe this transverse-like mode in $S(Q, E)$ for the liquid when performing scattering experiments at Q-values significantly smaller than in the case of the crystalline phase.

The indication of such strong similarities between the high-frequency dynamics of liquid and solid water, and, in particular, the interpretation of the weakly dispersing feature in the liquid as the manifestation of a transverse-like dynamics in a liquid system are certainly interesting and somewhat intriguing results. In fact, the need for a deeper investigation, and, eventually, also for an explanation of these findings based on more solid theoretical grounds are very evident—especially considering that the transition to a solid-like dynamics in a liquid at high frequencies, if confirmed, could be a very general property of the liquid state.

6. Longitudinal and transverse dynamics in liquid water

The discussion in the previous section indicates that the dynamics in liquid water is characterized by two branches, one strongly and the other weakly dispersing with Q. The first one has been identified as the sound branch with an upwards bend in the region below $Q = 4\ \mathrm{nm}^{-1}$. The second one, on the basis of INS and IXS results on ice crystals [33, 35, 36], has been related to a localized motion reminiscent of the transverse dynamics in the crystal. Similarly, from the analysis of MD simulations, this mode has been associated with the bending motion of three hydrogen-bonded water molecules. There are two important points still to be settled, however: (i) the physical mechanism(s) responsible for the bending of the sound branch and for the observation of a second mode at Q larger than $4\ \mathrm{nm}^{-1}$, and (ii) whether the behaviour of liquid water is common to a large class of liquids or is specific to this system. In this respect, one can hope to find some hints as regards these issues by studying the symmetry character, and its Q-dependence, of the modes observed in liquid water. This can be accomplished using the results of a numerical MD simulation of liquid water.

This point of view has motivated a recent large-scale MD simulation [37], where $N = 4000$ 'D_2O' SPC/E [38] molecules enclosed in a cubic box with periodic boundary conditions were considered [39]. The molar volume was 18 cm^3 and the temperature was $\approx$250 K, i.e. the temperature of maximum density for the SPC/E potential model [40]. In this calculation, the electrostatic long-range interactions were taken into account using the tapered reaction-field method, and the integration of the rotational equations of motion was carried out using an improved version of the Verlet algorithm [41]. The molecular trajectories, after achieving thermal equilibrium, were followed for $\approx$100 ps and stored every 10 fs, i.e. every five integration time steps. From the stored configurations, the instantaneous $\boldsymbol{Q}$-components of the density fluctuations of the centre of mass [42], $\rho_Q(t)$ (see equation (2)), were evaluated. The dynamic structure factor was then calculated from the power spectrum of $\rho_Q(t)$, i.e.

$$S(\boldsymbol{Q}, E) = |\mathcal{F}T\{\rho_Q(t)\}|^2. \tag{9}$$

To reduce the noise in $S(\boldsymbol{Q}, E)$, both a Hanning window and the Welsh method were utilized [44]. The time window was $\Delta t \approx 20$ ps, giving rise to an energy resolution of 0.04 meV. $S(\boldsymbol{Q}, E)$ has been averaged over independent directions of $\boldsymbol{Q} = (2\pi/L)(h, k, l)$ (where $L = 4.93$ nm is the box length) at several Q-values in the 1.3 to 35 nm^{-1} range.

The MD data have been directly compared to the IXS data. The match between the calculated function $S(Q, E)$, convoluted with the experimental resolution function, and the inelastic x-ray scattering data measured at 4 °C is very good for all of the Q-values investigated in the IXS experiment. As an example, in figure 13, we report the comparison at the selected Q-value of 4 nm^{-1}. The agreement between the calculated and measured spectra implies that the potential model used in the simulation is capable of representing the dynamics of real water at normal density successfully. Consequently, it is reasonable to expect that the transverse dynamics, a quantity which is not accessible to experiments, can also be reliably determined from the present MD data. The transverse and longitudinal current spectra have been calculated from the molecular trajectories as

$$C_L(Q, E) = E^2 S(Q, E)/Q^2 \tag{10}$$

and

$$C_T(\boldsymbol{Q}, E) = |\mathcal{F}T\{\boldsymbol{j}_Q^T(t)\}|^2 \tag{11}$$

where $\boldsymbol{j}_Q^T(t)$ is defined as

$$\boldsymbol{j}_Q^T(t) = \frac{1}{\sqrt{N}} \sum_j (\hat{\boldsymbol{Q}} \times (\hat{\boldsymbol{Q}} \times \boldsymbol{v}_j(t))) \exp(\mathrm{i}\boldsymbol{Q} \cdot \boldsymbol{R}_j(t)). \tag{12}$$

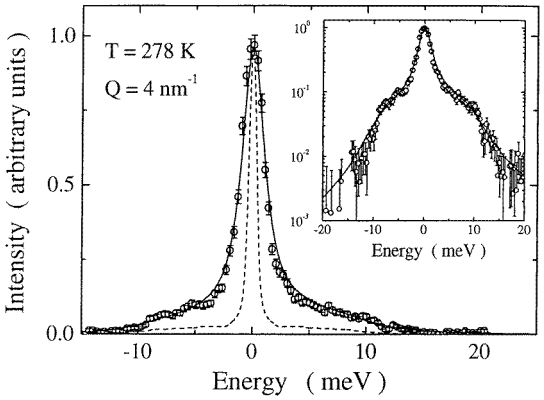

Figure 13. Comparison between the IXS data and the MD results at $T = 5\ ^{\circ}$C and $Q = 4\ \text{nm}^{-1}$. The IXS data (open circles) are reported with their error bars after subtraction of the instrumental background. The MD-calculated function $S(Q, E)$ (dashed curve) has been convoluted with the experimental resolution function, and the result (full curve) has been multiplied by an arbitrary scale factor in order to adjust the peak height to match the experimental data. The IXS and convoluted MD results are also reported in the inset, on a logarithmic scale, in order to show their good agreement in the tails of the spectrum also.

In figure 14 are reported examples of longitudinal (figure 14(a)) and transverse (figure 14(b)) current spectra at selected Q-values. Both of the current spectra, $C_L(Q, E)$ and $C_T(Q, E)$, show the existence of two excitations. The high-frequency excitation disperses with Q, and its sound velocity changes from $\approx$2000 m s^{-1} to $\approx$3300 m s^{-1}. This excitation appears at each Q-value in the longitudinal current spectra, while it is found in the transverse current spectra only at $Q > 4\ \text{nm}^{-1}$. We assign this feature to a quasi-longitudinal sound branch and we call it the L mode in view of its longitudinal character in the $Q \to 0$ limit. The behaviour of the low-frequency excitation is in some sense opposite: it is always present in the transverse current spectra, while it appears in the longitudinal current spectra only at $Q > 4\ \text{nm}^{-1}$. This low-frequency feature is from now on referred to as the T mode. At small Q, the T mode disperses with a sound velocity of $\approx$1500 m s^{-1}, and stays at an almost constant energy for $Q > 7\ \text{nm}^{-1}$.

The calculated spectra have been fitted with the same simple models as were used to fit the IXS data, and this allows us to summarize the excitations in terms of their energy ($\Omega_\eta(Q)$, $\eta = \{\text{L, T}\}$; i.e. the position of the current spectra maxima), their energy width ($\Gamma_\eta(Q)$), and their integrated intensity ($I_\eta(Q)$). Beside the DHO model, a more refined viscoelastic model has also been utilized [3], and values of the fitting parameters have been found which are consistent within their uncertainties. The best fits are superimposed on the MD data in figures 14(a), 14(b).

The values of the excitation energies, $\Omega_L(Q)$ and $\Omega_T(Q)$, are reported in figure 15. Figure 15(a) shows the complete Q-region investigated. The dispersion relation of the L modes follows the universal behaviour of liquid systems, i.e., a minimum appears at about the Q-value where $S(Q)$ attains its maximum. A similar minimum, although less pronounced, is found in the branch of the T modes. The figures 15(b), 15(c) give an expanded view of the dispersion in the small-momentum-transfer region. In figure 15(c) the change in slope of the L branch marks the transition between c_o and c_∞.

The MD results, comparing extremely well with the available INS and IXS data for liquid water reported in the previous sections, allow one to give emphasis to the point that, at

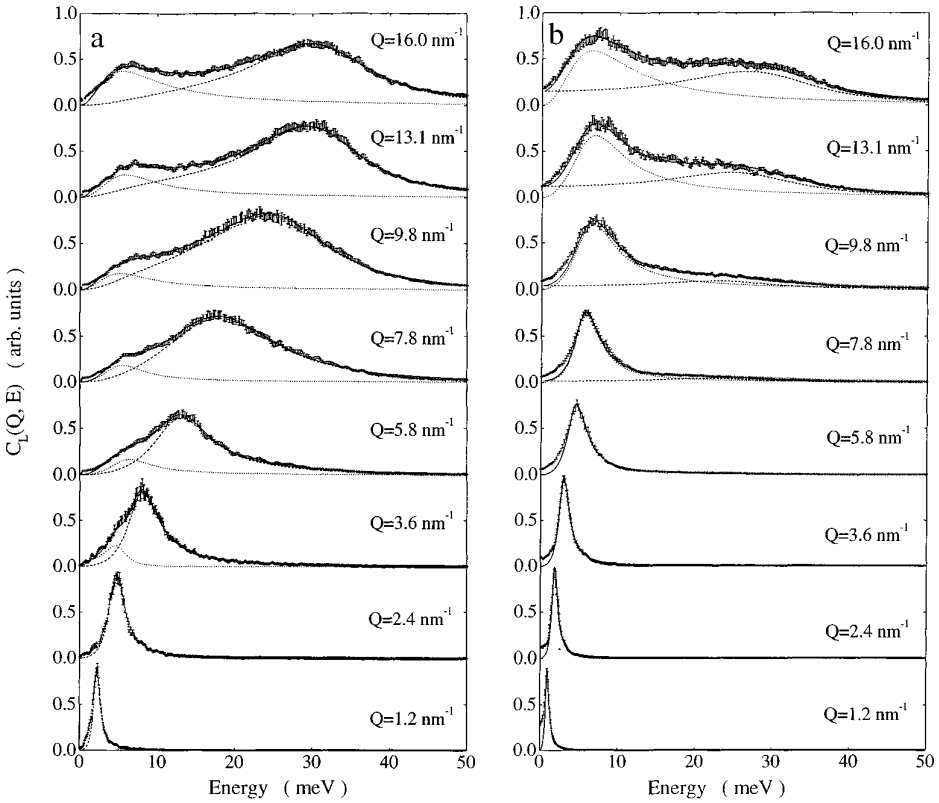

Figure 14. The longitudinal (a) and transverse (b) current spectra calculated from the MD simulation [37] are reported with their error bars at the Q-values indicated. The full curves are the best fits to the spectra. The dashed (dotted) curves show the individual contributions to the fit coming from the L mode (T mode).

energies below ≈30 meV, in the liquid, as in ice crystals, there are two phonon modes. As for the crystal, these are a longitudinal-like and a transverse-like phonon branch. Therefore, the MD results not only confirm that at Q larger than 4 nm^{-1} the longitudinal dynamics of liquid water becomes very similar to that of the crystalline solid, but also demonstrate that the second mode at ≈5–6 meV is due to a transverse-like dynamics. There is, however, an important difference between liquid and solid as regards the symmetry character of the two branches. In the solid, a dominant longitudinal or transverse character is preserved throughout the Q-region considered. In the liquid, the MD calculations show that, as a consequence of the lack of translational invariance, the pure symmetry character of the two modes is rapidly lost at large Q-values. Here, both modes contribute to similar extents to both the longitudinal, $C_L(Q, E)$, and the transverse, $C_T(Q, E)$, current spectra.

The MD results obtained at low Q, i.e. below 2 nm^{-1}, are consistent with the behaviour expected in a typical liquid system in the $Q \to 0$ limit, where only one mode is expected to survive in each current spectrum. In $C_L(Q, E)$, the L mode propagates with a velocity of sound approaching the hydrodynamic value measured in the macroscopic time- and length-scale limits. In $C_T(Q, E)$, the T mode loses its propagating character observed in the 2–4 nm^{-1} region, and one could infer that the transverse dynamics becomes progressively relaxational-like from the pile-up of spectral intensity towards zero frequency. The transition of the L mode

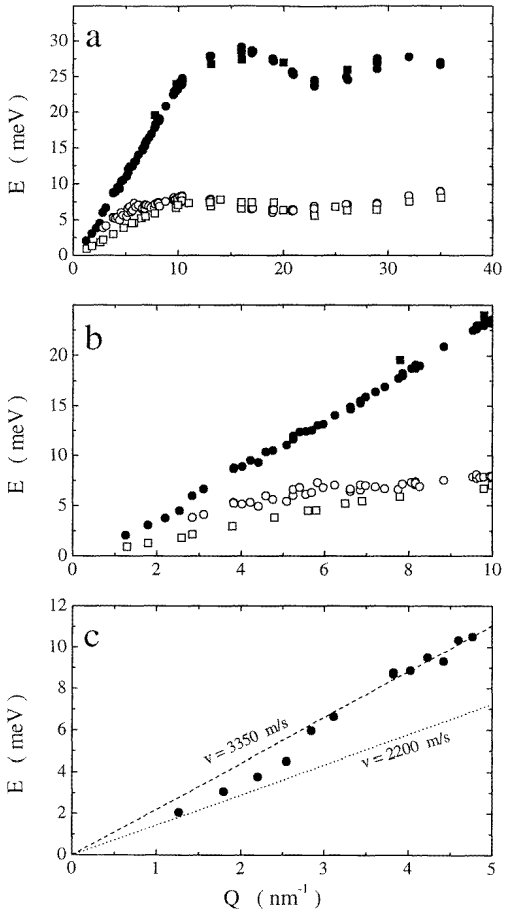

Figure 15. The energy positions of the L (full symbols) and T modes (open symbols) in three different Q-regions: (a) $Q = 0$–5 nm^{-1}; (b) $Q = 0$–10 nm^{-1}; (c) $Q = 0$–40 nm^{-1}. The circles (squares) represent the $\Omega_\eta(Q)$ parameter obtained from $C_L(Q,\omega)$ ($C_T(Q,\omega)$). The slopes of the lines in (c) correspond to the longitudinal v_o and v_∞ obtained using the present potential model.

to a pure longitudinal symmetry propagating with the c_o-value of the velocity of sound, and the disappearance of the T mode, bring the collective dynamics of liquid water back to the behaviour expected for a simple liquid in the macroscopic limit.

The transition from the low-frequency and low-Q hydrodynamic behaviour, where the density fluctuations propagate in a time- and space-averaged continuum medium, to the high-frequency solid-like regime, where the elastic response of the medium is dictated by the (disordered) instantaneous molecular arrangements, has already been observed in many glass-forming liquids [45]. This transition takes place at a Q-value where the frequency of the sound wave ω equals the inverse of the structural relaxation time τ. Manifestations of this transition include: (i) the increase of the longitudinal sound velocity from the low Q-value c_o towards its high Q-value c_∞; and (ii) the appearance of a propagating transverse dynamics. The condition $\omega\tau = 1$ is typically fulfilled at frequencies below 10^{10} Hz, depending on the temperature difference from the glass transition temperature of the system investigated. This behaviour is very similar to the one found here for liquid water. This is best summarized

in the Q-dependence of the parameters reported in figures 15, which can be scaled to the typical evolution of the sound velocity in a glass-forming liquid undergoing an α-relaxation process [45]. In contrast to the case for other known glass-forming systems, however, in water this transition would take place at much higher frequencies, $\approx 2.5 \times 10^{11}$ Hz, i.e. $\tau \approx 0.6$ ps. Finally, the wavelength marking the transition, $\lambda_\tau = 2\pi c_o \tau \approx 3$ nm, is comparable to the structural correlation length derived from $S(Q)$ measurements by Bosio *et al* [46]. A study of $S(Q, E)$ as a function of temperature could show whether the high-frequency dynamics of liquid water can be described within the same framework as was utilized for glass-forming systems. This can be understood by considering that the temperature change induces a steep modification of the parameter τ characterizing the structural α-relaxation, and therefore the frequency at which the transition from c_o to c_∞ would take place. In the next section, we will see that this is indeed the case, and that the transition can be associated with the structural relaxation due to the making and breaking of the hydrogen bonds.

7. Temperature dependence of the high-frequency dynamics in liquid water

In glass-forming liquids the transition between the viscous regime at low frequency and the elastic one at high frequency is determined by the coupling of the propagating density fluctuations with the dynamics of the structural rearrangements of the particles in the liquid. Such a complex dynamics, taking place at the atomic scale, and giving rise to the local rearrangements, can be described by a relaxation process with a characteristic time τ. For glass-forming liquids, τ has a strong temperature dependence; close to the melting point typical values of τ are in the *nano*second range; it dramatically increases on lowering the temperature, and near the calorimetric glass transition temperature T_g it reaches values as high as hundreds of seconds [47]. As was mentioned in the previous section, this structural relaxation process has a cooperative nature, and the density fluctuations are differently influenced in the two opposite frequency limits: the system has a solid-like elastic behaviour for $\omega\tau \gg 1$, and a viscous one for $\omega\tau \ll 1$. Along these lines, one could speculate that for liquid water the physical mechanism responsible for the dispersion of the sound velocity is also an α-relaxation process. However, a few important differences exist between water and the majority of the systems belonging to the class of glass formers. Indeed, unlike the case for the latter systems, for water the existence of a liquid-to-glass transition, predicted to occur in the 130–140 K region, has not yet been firmly established. The situation is in fact even more involved, as extrapolation from results of experiments carried out at $T > 245$ K and molecular dynamics simulations seem to indicate the presence of a relaxation time that diverges at $T \approx 230$ K [6]. A further quantitative difference is found in the characteristic time, which in water is in the *pico*second range at the liquid-to-crystal transition, i.e. much smaller than those for glass formers at their melting temperatures.

The experimental characterization of the α-process is typically obtained by the determination of the dispersion of the sound velocity as a function of T and at a constant Q-transfer value. At the inflection point (t) of such an 'S'-shaped curve, the condition $\Omega_t(Q, T)\tau(T) \approx 1$, with $\Omega(Q, T) = c_{app}(Q, T)Q$, is fulfilled. In glass-forming liquids, this condition is met by Brillouin light scattering (BLS) measurements close to melting, and by ultrasonic (US) methods close to T_g. Indeed, the typical frequencies allowed by these two techniques are such that $\Omega_t(Q, T)\tau(T) \approx 1$.

In the case of water, as a consequence of the small value of τ close to the crystal melting temperature, BLS cannot access the relevant excitation energy region, although, in the highly supercooled liquid, it was possible to detect by means of BLS a deviation of c_o towards a higher value, i.e. towards c_∞ [22, 23]. The complete determination of the 'S'-shaped curve

as a function of either T or Q requires, however, the use of IXS. Using the IXS technique, therefore, one can determine the inflection point in the c–Q curve, and, consequently, the relaxation time τ.

These observations motivated an IXS study on the temperature dependence of the transition from normal to fast sound in liquid water. The temperature- and momentum-transfer ranges considered were, respectively, the $T = 260$–570 K and $Q = 1$–12 nm^{-1} regions [48]. In order to emphasize the thermal effects, and to minimize the modification of the hydrogen-bond dynamics due to large variations of the excluded volume, in this experiment the density was kept as constant as possible within the experimental capabilities by adjusting the pressure in the 0–2 kbar range. The IXS spectra were measured at different (Q, T, P) points. The Q-dependence was studied in the 1–12 nm^{-1} region at temperatures of 278, 373, and 493 K. The T-dependence was studied at the Q-values of 2, 4, and 7 nm^{-1} in the 260–570 K region. The pressure, selected according to the equation of state (EOS) [49], was varied to maintain the density, $\rho \approx 1.00$ g cm^{-3}. The points at $T < 270$ K were taken at $P = 2$ kbar, corresponding to $\rho \approx 1.02$–1.07 g cm^{-3}, while for those measured at $T > 410$ K, also taken at $P = 2$ kbar, the density was in the range $\rho \approx 1.00$–0.96 g cm^{-3}.

An example of the evolution observed in the IXS spectra as a function of temperature is reported in figure 16 for $Q = 2$ and 4 nm^{-1} and three selected temperatures together with their fits, performed as for the water spectra discussed in the fourth and fifth sections. The energy dispersion of the inelastic signal with Q is reported in figure 17 at the selected temperatures of 278, 373, and 493 K. One observes that the deviation of the dispersion curve from the straight line, whose slope corresponds to c_o as obtained from the EOS, takes place at increasing Q-values with increasing temperatures. In figure 17 this has been emphasized by plotting the three dispersion curves on top of each other. In this figure, the values of $\Omega(Q, T)$ have been scaled by the ratio $c_o(278\text{ K})/c_o(T)$, where c_o is the adiabatic sound velocity obtained from the equation of state (EOS) [49], and the full line represents the adiabatic sound dispersion $\Omega(Q) = c_o(278\text{ K})Q$. The scaling of the excitation energy to the adiabatic sound velocity at $T = 278$ K allows us to emphasize that the transition of the apparent sound velocity $\Omega(Q)/Q$ from the adiabatic c_o-value to the high-frequency limit, c_∞, takes place at a Q-value which is strongly temperature dependent. In the dispersion at $T = 278$ K, the deviation from c_o can already be observed at $\approx$1 nm^{-1}, while, at $T = 373$ K and $T = 493$ K, this deviation is observed at Q-values larger than 3 and 6 nm^{-1} respectively.

The behaviour summarized in figures 16 and 17 provides experimental evidence that the mechanism underlying the observed transition has a dynamical origin, and, in fact, is likely to be due to a relaxation process. The temperature dependence of its characteristic relaxation time, τ, is then the cause of the strong temperature dependence of the Q-value, Q_t, at which the transition is observed.

A quantitative determination of both Q_t and τ can be made by introducing the apparent longitudinal elastic modulus: $M = \rho_W c^2(Q, T)$ (here ρ_W is the mass density). In the simple Debye approximation for the relaxation process, the frequency dependence of M, leading to the dispersion from its low-frequency value $M_o = \rho_W c_o^2$ to its high-frequency one $M_\infty = \rho_W c_\infty^2$, is given by [50]

$$M = M_\infty + \frac{M_o - M_\infty}{1 + \mathrm{i}\omega\tau}. \tag{13}$$

Introducing the *reduced* apparent modulus M_r:

$$M_r = \frac{M - M_o}{M_\infty - M_o} \tag{14}$$

the values of τ can be determined from the condition $\mathrm{Re}(M_r) = 0.5$. The calculation of $M_r(Q, T)$ from the measured apparent sound velocity requires the knowledge of c_o and c_∞.

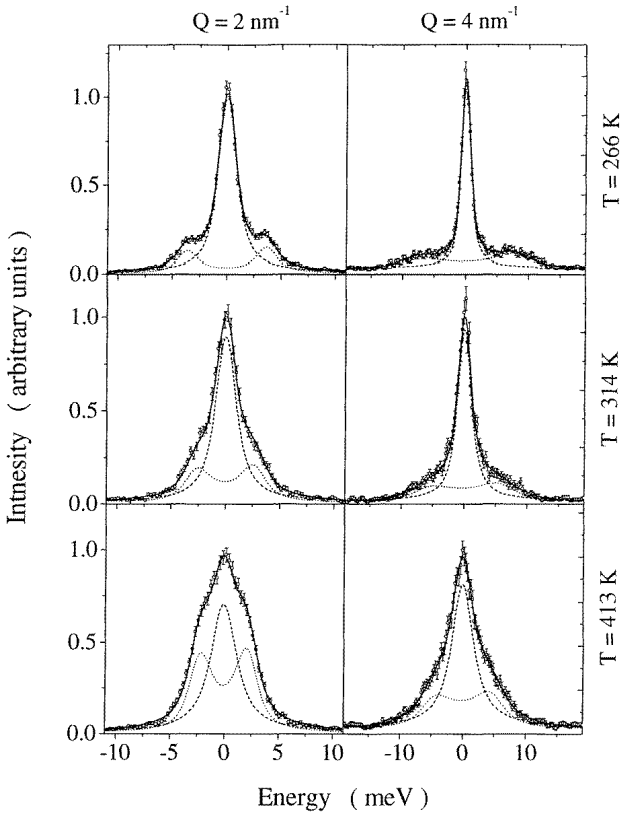

Figure 16. Examples of IXS spectra of liquid water at the Q- and T-values indicated (open circles) shown together with the total fits and the individual components. The spectra at $T = 266$ (314, 413) K were taken at $P = 2$ (0.3, 2) kbar, corresponding to the densities $\rho = 1.02$ (1.00, 0.98) g cm^{-3}.

For $c_o(T)$, we used the values from the EOS [49] and we assumed them to be Q-independent; this hypothesis is justified by the small variation of the static structure factor in the Q-range considered [9, 51]. We also assumed a T- and Q-independent value of $c_\infty = 3200$ m s^{-1} (derived from the IXS measurements at $T = 278$ K [33]). In deriving $M_r(Q, T)$, one must also consider that $c(Q, T)$ could depend on the model utilized for $S(Q, E)$. Within these approximations, we obtained, from the data reported in figures 16 and 17, the M_r-values shown in figure 18. This allows us to determine the momentum-transfer value Q_t from the condition $M_r = 0.5$ at the temperature considered. The values for $\tau(T)$ are then derived as $\tau(T) = \Omega(Q_t, T)^{-1}$, where $\Omega(Q_t, T)$ is obtained by interpolating $\Omega(Q, T)$ reported in figure 17. Similarly, from the sets of measurements performed at $Q = 2$, 4, and 7 nm^{-1} as functions of temperature, we obtained the values of $\Omega(Q, T)$ which lead to the values of $M_r(Q, T)$ reported in figure 19. Here, from the condition $M_r(Q, T) = 0.5$, we obtained the temperature T_t, where the selected momentum transfer becomes Q_t. Therefore $\tau(T) = \Omega(Q, T_t)^{-1}$, where $\Omega(Q, T_t)$ is obtained by interpolating $\Omega(Q, T)$.

The values of $\tau(T, Q)$ derived from figures 18 and 19 are reported in figure 20. This quantity changes from 1.3 ps at 280 K to 0.2 ps at 490 K. In spite of the fact that the present measurements were performed at constant density, the derived τ-values are consistent with

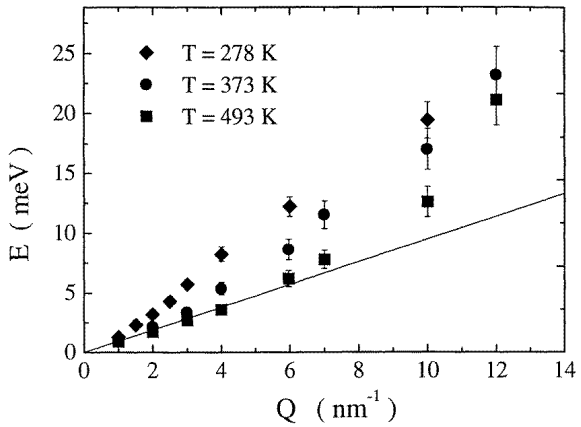

Figure 17. The dispersion relation of the $\Omega(Q)$ parameter as a function of Q at $T = 278$ K (full diamonds), 373 K (full circles), and 493 K (full squares). The excitation values have been scaled by the factor $c_o(278\text{ K})/c_o(T)$, with values of $c_o(T)$ obtained from the EOS [49]. This has been done to emphasize, in the same plot, the departure of the dispersion relation from the $c_o(T)Q$ law, shown by the solid line, which is valid in the $Q \to 0$ limit. This departure takes place at increasing Q-values with increasing temperatures.

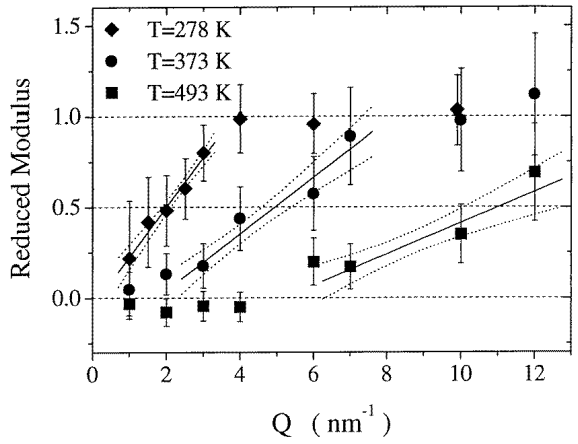

Figure 18. The Q-dependence of the reduced apparent modulus, M_r, at the temperatures indicated (the key to the symbols is as for figure 17). The Q-values at which the transition take place, Q_t, have been determined from the condition $M_r = 0.5$. This has been found by means of linear fits to the data, shown (full lines) together with their $\pm 1\ \sigma$ prediction bands (dotted curves).

other determinations performed along the coexistence curve. This is shown in figure 20, where we also report the τ-values obtained from the linewidths of the depolarized Raman scattering [52, 53]. These values are also comparable to those obtained from ultrasound absorption and viscosity measurements [54], Brillouin light scattering data [22, 23], and molecular dynamics simulations [19]. In the temperature- and momentum-transfer region considered, we also observe that τ does not have a marked Q-dependence, and, when fitted to an Arrhenius behaviour, gives an activation energy $\Delta E = 2.5 \pm 0.5$ kcal mol^{-1}. This value is consistent with the other determinations along the coexistence curve, where a relevant

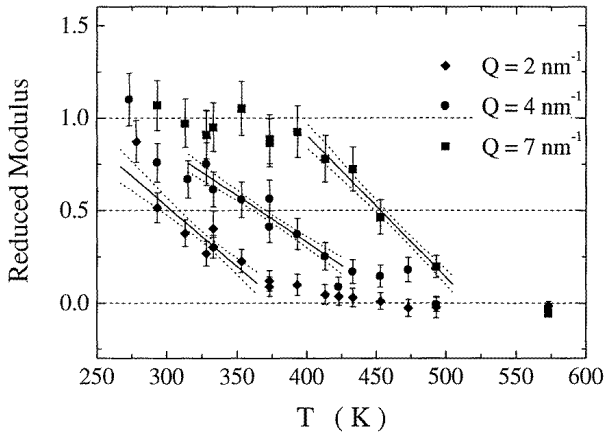

Figure 19. The T-dependence of the reduced apparent modulus, M_r, at $Q = 2$ nm^{-1} (full diamonds), 4 nm^{-1} (full circles), and 7 nm^{-1} (full squares). The values of the transition temperature, T_t, have been determined in the same way as the Q_t-values in figure 18.

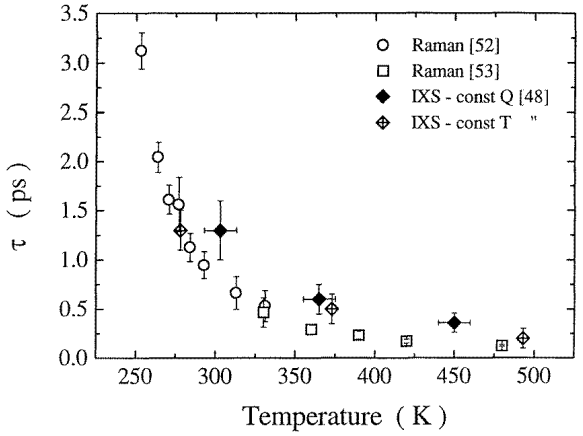

Figure 20. The relaxation time τ as obtained from the analysis of the apparent reduced moduli reported in figures 18 (crossed diamonds) and 19 (full diamonds) are shown together with those derived from depolarized Raman scattering in references [52] (open circles) and [53] (open squares).

deviation from the Arrhenius behaviour is observed only at temperatures below 280 K.

Summarizing the work reported in this section, the study of the temperature dependence of $S(Q, E)$ for liquid water has shown that the transition between the low-frequency adiabatic sound velocity towards its high-frequency limit takes place at a Q_t-value which is strongly temperature dependent. This demonstrates that such a transition is due to a relaxation process. Moreover, the phenomenology found in the temperature and Q-dependencies of the excitation energies of the longitudinal sound mode strongly resembles that observed for glass-forming liquids undergoing the α-relaxation process, although on a much faster timescale. Consequently, this similarity leads us to suppose that in water, the relaxation process leading to the transition considered is also due to a rearrangement of the local molecular structure.

8. Conclusions

The study of the high-frequency dynamics in liquid water, reviewed in this article, is beginning to provide a satisfactory picture of the characteristic excitations of this system in the region corresponding to the molecular motion at the interparticle distance level. Most important, from the previous discussion one also starts to have a reasonable picture of the physical mechanisms affecting the momentum and temperature dependences of these excitations. A very large body of theoretical, numerical simulation, and experimental work has been dedicated to the study of the collective dynamical properties of liquid water during the last twenty years or more. In the present article, we have reviewed the main results of this earlier work, and we have tried to put them into perspective with the new experimental determinations of the dynamic structure factor of liquid water obtained thanks to the development of the inelastic x-ray scattering method with meV energy resolution.

The use of the IXS technique, more specifically, has allowed a few important points on the collective dynamic of water to be clarified. In particular, we have seen that:

- The fast-sound excitation branch is clearly observed by means of IXS, confirming the earlier neutron work of Teixeira *et al* [11]. Using the sensitivity of IXS to the oxygen atom, and therefore the fact that the IXS signal is completely dominated by the O–O correlation function, the IXS results have established that the fast sound is a property of the centre of mass of the whole water molecule, and not some exotic excitation involving mainly the motion of the lighter hydrogen atoms.
- The simultaneous existence of two modes, as predicted from the molecular dynamics calculations, has been demonstrated for Q larger than 4 nm^{-1}: the low-frequency mode has a weakly dispersing character and corresponds to a transverse-like dynamics, while the other mode corresponds to the longitudinal acoustic branch whose sound velocity at high frequency corresponds to the fast sound. These two important conclusions arise from a direct comparison between the IXS data for liquid water with those measured for solid water (ice I_h), and with those obtained by a large-scale molecular dynamics simulation, which allowed a symmetry analysis as a function of Q of the two modes. A direct consequence of these studies is the experimental observation that the high-frequency collective dynamics of liquid water is equivalent to that of its solid-state counterpart. This conclusion, associated with the knowledge that the local structure of liquid water is characterized by a tetrahedral coordination almost identical to that of the solid, tells us that density fluctuations in the picosecond range in liquid water at ambient conditions evolve as in an ice I_h structure, and therefore they are very weakly coupled to the degrees of freedom characteristic of the liquid state: diffusion and molecular reorientation processes.
- The previous point has motivated a detailed IXS study of $S(Q, E)$ for liquid water as a function of Q and temperature at essentially constant density. This work has demonstrated that, at constant temperature, there exists a positive dispersion of the velocity of sound in the longitudinal dynamics, whose value evolves in a narrow Q-region from the ordinary sound value at low Q to the high-frequency 'fast' value at high Q. The transverse-like excitation, observed at 4–6 meV and weakly depending on Q, is observed only in the high-frequency limit, i.e. when the solid-like behaviour has been reached and the longitudinal-like excitations propagate with the 'fast' sound. The transition between ordinary and fast sound is found to be very much dependent on temperature. Specifically, it is found to move towards higher Q-values when increasing temperature. These experimental results closely follow previous predictions made on the basis of molecular dynamics simulations. Moreover, they confirm the suggestion that the transition between the two sound velocities can be described within the theoretical framework of the α-relaxation process, which has

been developed to describe a similar dispersion in the sound velocity found in glass-forming liquids. Unlike the case for these systems, however, for liquid water close to melting, the frequency range of this transition is one to two orders of magnitude higher. In this framework, the fast sound corresponds to the infinite sound velocity c_∞, and the ordinary sound velocity to the zero-frequency sound velocity c_o. In this picture, the physical mechanism responsible for the transition from c_o to c_∞ is a rearrangement of the local structure taking place in a liquid with a characteristic relaxation time τ. Considering density fluctuations which have a timescale long with respect to τ, the liquid is in a completely relaxed state, the vibrational and relaxational degrees of freedom are in thermodynamical equilibrium, and the predictions of the hydrodynamics theory can be applied. In the opposite limit, when the density fluctuations are fast with respect to τ, the vibrational degrees of freedom cannot exchange energy with the relaxational ones; the constituent particles behave as if they were displaced from their equilibrium positions (that 'slowly' change with time as dictated by the relaxational dynamics) by the vibrational degrees of freedom: in this sense, the collective dynamics of the liquid is seen as solid-like. The use of a simple model, based on a Debye *ansatz* to visualize the relaxation of the elastic modulus, has allowed us to extract the value of τ as a function of temperature (hereafter we neglect a possible Q-dependence of τ). The derived values are consistent with previous determinations based on the width of the central peak as measured by the depolarized Raman technique. Finally, in the temperature range investigated, the values of τ are also consistent with an Arrhenius behaviour: the associated activation energy is found to be comparable to the hydrogen bonding energy of two water molecules. Consequently, one could speculate that the relaxation mechanism lying at the origin of the transition from c_o to c_∞ is determined by the structural rearrangement due to the making and the breaking of hydrogen bonds. This appealing idea, important because it would provide a direct means to study the role of the hydrogen bond in the microscopic dynamics of hydrogen-bonded systems, is at present only a hypothesis. The construction of specific models for $S(Q, E)$, such as those based on the viscoelastic theory [55], or on the kinetic theory [56], will allow one to extract more reliable values of the parameters governing the relaxation process, such as $\tau(Q, T, \rho)$ and the strength of the relaxation process itself. The quality of the data, and the number of thermodynamical points are beginning to be respectively sufficiently accurate and sufficiently numerous, and in fact some of this analysis work is already in progress [55, 56].

In conclusion, the present article, giving a review of our present understanding of the high-frequency dynamics of liquid water, has also shown how the new IXS technique can contribute to the study of unsettled issues in the dynamics of liquids in general. The IXS technique is, in fact, an experimental method enabling the dynamic structure factor, or, at least, some crucial parts of it, to be measured. This method, as in the case of well established ones such as numerical simulation and neutron scattering, provides the possibility of studying from a new and different point of view the collective dynamics of liquids and disordered systems in general. We expect, therefore, that with IXS it will be possible to contribute to a better determination of the interparticle potentials and to improve our understanding of a few unsettled issues, such as those relating certain macroscopic properties of disordered materials to their microscopic structure and dynamics.

We conclude this article by going back to water, and noticing how little is known still on the origin of the many stable and metastable phases of this molecule in both its liquid, super-critical fluid, and solid forms [8]. It is our hope that this very active field of research will benefit from the application of the IXS method for investigating the microscopic dynamics of the H_2O molecules as a function of their thermodynamic state.

Acknowledgments

The IXS work presented here was possible thanks to the collaboration with U Bergmann, A Cunsolo, M Krisch, C Masciovecchio, V Mazzacurati, A Mermet, G Monaco, M Sampoli, G Signorelli, and R Verbeni. We also greatly benefited from useful discussions with U Balucani, M C Bellisent-Funel, S H Chen, M Nardone, Y Petroff, F Sciortino, H E Stanley, J Teixeira and G Viliani.

We also would like to acknowledge those who contributed to the development of the new IXS spectroscopic tool on the ID16 beamline at the ESRF. In particular, the construction and operation of BL21-ID16 has been possible thanks to the technical help of B Gorges, K Martel, and J F Ribois from the ESRF, and O Consorte and W Galli, from the Brillouin Spectroscopy Group of the University of L'Aquila.

References

[1] Hansen J-P and McDonald I R 1976 *Theory of Simple Liquids* (London: Academic)
[2] Egelstaff P A 1994 *An Introduction to the Liquid State* 2nd edn (Oxford: Clarendon)
[3] Balucani U and Zoppi M 1994 *Dynamics of the Liquid State* (Oxford: Oxford Science)
[4] Alley W E, Alder B J and Yip S 1983 *Phys. Rev.* A **27** 3174
Bruin C, Michels J P J, Van Rijs J C, de Graaf L A and deSchepper I M 1985 *Phys. Lett.* A **110** 40
[5] deSchepper I M, Van Rijs J C, van Well A A, Verkerk P and de Graaf L A 1984 *Phys. Rev.* A **29** 1602
Bafile U, Barocchi F, Neumann M and Verkerk P 1994 *J. Phys.: Condens. Matter* **6** A107
[6] Debenedetti P G 1997 *Metastable Liquids* (Princeton, NJ: Princeton University Press) pp 330–5
[7] Angell C A 1983 *Annu. Rev. Phys. Chem.* **34** 593 and references therein
Angell C A 1995 *Science* **267** 1924
[8] Mishima O and Stanley H E 1998 *Nature* **396** 329 and references therein
[9] Rahman A and Stillinger F H 1974 *Phys. Rev.* A **1** 368
[10] Bosi P, Dupré F, Menzinger F, Sacchetti F and Spinelli M C 1978 *Nuovo Cimento Lett.* **21** 436
[11] Teixeira J, Bellissent-Funel M C, Chen S H and Dorner B 1985 *Phys. Rev. Lett.* **54** 2681
[12] Impey R W, Madden P A and McDonald I R 1982 *Mol. Phys.* **46** 513
[13] Wojcik M and Clementi E 1986 *J. Chem. Phys.* **85** 6085
[14] Ricci M A, Rocca M D, Ruocco G and Vallauri R 1988 *Phys. Rev. Lett.* **61** 1958
[15] Ricci M A, Rocca M D, Ruocco G and Vallauri R 1989 *Phys. Rev.* A **40** 7226
[16] Sastry S, Sciortino F and Stanley E 1991 *J. Chem. Phys.* **95** 7775
[17] Balucani U, Ruocco G, Sampoli M, Torcini A and Vallauri R 1993 *Chem. Phys. Lett.* **209** 408
[18] Balucani U, Ruocco G, Torcini A and Vallauri R 1993 *Phys. Rev.* E **47** 1677
[19] Sciortino F and Sastry S 1994 *J. Chem. Phys.* **100** 3881
[20] Tozzini V and Tosi M P 1996 *Phys. Chem. Liq.* **33** 191
[21] Balucani U, Brodholt J P and Vallauri R 1997 *J. Phys. C: Solid State Phys.* **8** 9269
[22] Magazú S, Maisano G, Majolino D, Mallamace F, Migliardo P, Aliotta F and Vasi C 1989 *J. Chem. Phys.* **93** 942
Maisano G, Migliardo P, Aliotta F, Vasi C, Wanderlingh F and D'Arrigo G 1984 *Phys. Rev. Lett.* **52** 1025
[23] Cunsolo A and Nardone M 1996 *J. Chem. Phys.* **105** 3911
[24] Bermejo F J, Alvarez M, Bennington S M and Vallauri R 1995 *Phys. Rev.* E **51** 2260
[25] Ruocco G and Sette F 1998 *Bull. Soc. Fr. Physique* **115** 26
[26] Zachariasen H 1944 *Theory of X-ray Diffraction in Crystals* (New York: Dover)
[27] A perfect crystal can be defined as a periodic lattice without defects and/or distortions in the reflecting volume capable of inducing relative variations of the distance between the diffracting planes, $\Delta d/d$, larger than the desired relative energy resolution: within this volume $\Delta d/d \ll (\Delta E/E)_h \approx 10^{-8}$. This stringent requirement practically limits the choice of the material to realize the monochromator and analyser crystals capable of reaching meV energy resolutions from 20 keV x-rays to silicon. The highest resolving power reached so far using Bragg reflections in a perfect crystal is $\Delta E/E = 1 \times 10^{-8}$, and it has been reached on the BL21-ID16 beamline at the ESRF utilizing a silicon crystal operating at the $\boldsymbol{Q}_h = 2\pi/a_{\mathrm{Si}(13\,13\,13)} = 260.5\ \mathrm{nm}^{-1}$ reflection order ($a_{\mathrm{Si}} = 0.5431$ nm being the lattice parameter of crystalline silicon) and x-ray photons of energy ≈26 keV ($\theta_B \approx 89.98^\circ$).
Verbeni R, Sette F, Krisch M H, Bergmann U, Gorges B, Halcoussis C, Martel K, Masciovecchio C, Ruocco G and Sinn H 1996 *J. Synchrotron Radiat.* **3** 62

[28] Bottom V E 1965 *An. Acad. Bras. Cienc.* **37** 407
[29] Maier-Leibnitz H 1966 *Nucleonik* **8** 61
[30] Masciovecchio C, Bergmann U, Krisch M H, Ruocco G, Sette F and Verbeni R 1996 *Nucl. Instrum. Methods* B **111** 181
Masciovecchio C, Bergmann U, Krisch M H, Ruocco G, Sette F and Verbeni R 1996 *Nucl. Instrum. Methods* B **117** 339
[31] Sette F, Ruocco G, Krisch M, Bergmann U, Masciovecchio C, Mazzacurati V, Signorelli G and Verbeni R 1995 *Phys. Rev. Lett.* **75** 850
[32] Ruocco G, Sette F, Krisch M, Bergmann U, Masciovecchio C, Mazzacurati V, Signorelli G and Verbeni R 1996 *Nature* **379** 521
[33] Sette F, Ruocco G, Krisch M, Masciovecchio C, Verbeni R and Bergmann U 1996 *Phys. Rev. Lett.* **77** 83
[34] Fak B and Dorner B 1992 *Institute Laue–Langevin (Grenoble) Technical Report* No 92FA008S
[35] Renker B 1969 *Phys. Lett.* A **30** 493
[36] Ruocco G, Sette F, Krisch M, Bergmann U, Masciovecchio C and Verbeni R 1996 *Phys. Rev.* B **54** 14 892
[37] Sampoli M, Ruocco G and Sette F 1997 *Phys. Lett.* **79** 1678
[38] Berendsen H J C, Postma J P M, Van Gunsteren W F and Hermans H J 1981 *Intermolecular Forces* ed B Pulmann (Dordrecht: Reidel) p 331
[39] 'D_2O' molecules have been preferred over 'H_2O' molecules for their higher moments of inertia, enabling longer integration time steps of the equation of motion to be employed in the microcanonical ensemble.
[40] Poole P H, Sciortino F, Essmann U and Stanley H E 1993 *Phys. Rev.* E **48** 3799
[41] Ruocco G and Sampoli M 1994 *Mol. Phys.* **82** 875
Ruocco G and Sampoli M 1995 *Mol. Simul.* **15** 281
[42] In this article we discuss the density fluctuations at the centre-of-mass level, and we compare them with the results from IXS experiments that are mainly sensitive to the oxygen-density fluctuations. This is justified by the near coincidence of the centre of mass and oxygen position in the water molecule. Other experiments, real and simulated, are more sensitive to the orientational dynamics, and, therefore, relate to the hydrogen current spectra (e.g., see reference [43]).
[43] Bertolini D and Tani A 1992 *Mol. Phys.* **75** 1047
[44] Welsh P D 1967 *IEEE Trans. Audio Electroacoust.* A **15** 70
Hayes M H 1996 *Statistical Digital Signal Processing and Modelling* (London: Wiley)
[45] Dianoux A J, Petry W and Richter D (ed) 1993 *Dynamics of Disordered Materials* II (Amsterdam: North-Holland)
[46] Bosio L, Teixeira J and Stanley H E 1981 *Phys. Rev. Lett.* **46** 597
[47] Angell C A 1995 *Science* **267** 1924
[48] Cunsolo A, Ruocco G, Sette F, Masciovecchio C, Mermet A, Monaco G, Sampoli M and Verbeni R 1999 *Phys. Rev. Lett.* **82** 0000
[49] Kestin J and Senger J V 1986 *J. Phys. Chem. Ref. Data* **15** 305
[50] Herzfeld K F and Litovitz T A 1959 *Absorption and Dispersion of Ultrasonic Waves* (New York: Academic)
[51] Bertolini D and Tani A 1995 *Phys. Rev.* E **51** 1091
Bertolini D and Tani A 1995 *Phys. Rev.* E **52** 1699
Bertolini D and Tani A 1997 *Phys. Rev.* E **56** 4135
[52] Mazzacurati V, Nucara A, Ricci M A, Ruocco G and Signorelli G 1990 *J. Chem. Phys.* **93** 7767
[53] Fontana A, Nardone M and Ricci M A 1995 *J. Chem. Phys.* **102** 6975
[54] Hie W M, Doylor A R and Litovitz T A 1966 *J. Chem. Phys.* **44** 3712
Davis C M and Jarzynki J 1972 *Water: a Comprehensive Treatise* vol 1, ed F Frank (New York: Plenum) pp 443–61
[55] Monaco G, Cunsolo A, Ruocco G and Sette F 1999 *Phys. Rev.* E at press
[56] Chen S H, Liao C, Sciortino F and Sette F 1999 *Phys. Rev.* E at press